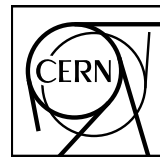


EUROPEAN ORGANIZATION FOR NUCLEAR RESEARCH



CERN-EP-2019 -XXX
Day Month 2019

AK femtoscopy in Pb-Pb collisions at $\sqrt{s_{\text{NN}}} = 2.76 \text{ TeV}$

ALICE Collaboration*

Abstract

We present the first measurement of the scattering parameters of AK pairs in all three charge combinations (ΛK^+ , ΛK^- , and ΛK_S^0). We achieve the measurements through our femtoscopic analysis of AK correlations in Pb-Pb collisions at $\sqrt{s_{\text{NN}}} = 2.76 \text{ TeV}$ from ALICE. The femtoscopic correlations result from strong final-state interactions, and are fit with a parametrization allowing us to both characterize the pair emission source and measure the scattering parameters for the particle pairs. The fit assumes a common radius and λ parameter for each centrality bin, shared across all AK pair systems. We perform an extensive study with the THERMINATOR 2 event generator to account for both non-femtoscopic backgrounds, as well as contributions from residual correlations induced by feed-down from resonances. We find the non-femtoscopic background is due almost entirely to collective effects, and we are able to use the event generator to quantitatively describe it with unprecedented precision. In the experimental data, we observe a striking difference between the ΛK^+ and ΛK^- correlations in pairs with low relative momenta ($k^* \lesssim 100 \text{ MeV}$). The ΛK^+ system exhibits a negative real component of the scattering parameter ($\Re f_0$), while that of the ΛK^- is positive. The underlying cause dictating this interesting difference arises from the different quark content upon which the strong interaction depends. The results might suggest an effect arising from different quark-antiquark interactions between the pairs ($s\bar{s}$ in ΛK^+ and $u\bar{u}$ in ΛK^-), or from different net strangeness for each system ($S=0$ for ΛK^+ , and $S=-2$ for ΛK^-). Finally, we find that the AK systems exhibit source radii larger than expected from extrapolation from identical particle femtoscopic studies. We interpret this effect as resulting from the separation in space-time of the single-particle Λ and K source distributions.

© 2019 CERN for the benefit of the ALICE Collaboration.

Reproduction of this article or parts of it is allowed as specified in the CC-BY-4.0 license.

*See Appendix F for the list of collaboration members

26 1 Introduction

27 Femtoscopy is an experimental method used to study the space-time characteristic of the particle emitting
 28 sources in relativistic particle collisions [1]. With this method, two(or many)-particle relative-momentum
 29 correlation functions are used to connect the final-state momentum distributions to the space-time distri-
 30 butions of particle emission at freeze-out. The correlation functions are sensitive to quantum statistics, as
 31 well as strong and Coulomb final-state interactions (FSI). In addition to characterizing the source region,
 32 femtoscopy offers a unique opportunity to measure nuclear scattering parameters, many of which are dif-
 33 ficult, if not impossible, to measure otherwise. In many pair systems, the contributions to the correlation
 34 function from quantum statistics and/or the Coulomb interaction overwhelm that of the strong interac-
 35 tion, making it difficult to extract scattering information. In this article, we study Λ-K pairs, in which
 36 at least one particle is electrically neutral. Therefore, quantum statistics and the Coulomb interaction do
 37 not contribute, giving us a clear signal from the strong interaction.

38 Femtoscopic analyses of pions, kaons, and protons have revealed a trend of decreasing source radii with
 39 increasing transverse mass [2], which, for identical particle pairs, is defined as $m_T^2 = m^2 + k_T^2$, where
 40 $k_T = \frac{1}{2}|\mathbf{p}_{T,1} + \mathbf{p}_{T,2}|$. This effect is interpreted as a signature of hydrodynamic flow in the heavy-ion
 41 collisions [3]. The exponent for m_T -scaling can be shown analytically to be $-\frac{1}{2}$ for case of a one-
 42 dimensional longitudinal hydrodynamic expansion with negligible transverse flow and common freeze-
 43 out characteristics, regardless of particle species. This has lead to an idea of universal m_T -scaling for
 44 different particle species. However, it is unclear how the picture changes with significant transverse flow,
 45 viscosity corrections, and hadronic rescattering. Additionally, the scaling observed in models exists
 46 separately for the three-dimensional radii in the Longitudinally Co-Moving System (LCMS), and will at
 47 best only be approximate in the Pair Rest Frame (PRF) [2, 4].

48 The radii we extract from our study are larger than one would expect from naively following the trends
 49 set forth in the identical particle analyses. However, when dealing with non-identical particles, such
 50 as in the present case with ΛK pairs, we should not necessarily expect the exact same trend. In such
 51 cases, the pair emission source, measured through femtoscopy, is the superposition of two single-particle
 52 sources, each with its own unique size, shape, and space-time position within the medium. Although the
 53 single-particle sources should abide by the approximate m_T -scaling, the pair sources generally will not.

54 This paper presents the first measurement of the scattering parameters of ΛK pairs in all three charge
 55 combinations (ΛK^+ , ΛK^- , and ΛK_S^0). The scattering parameters, along with pair emission source sizes,
 56 are extracted with a femtoscopic analysis of ΛK correlations in Pb-Pb collisions at $\sqrt{s_{NN}} = 2.76$ TeV
 57 from ALICE experiment at the LHC. These correlations result from strong final-state interactions, and
 58 are fit with a parametrization by Lednický and Lyuboshitz [5]. We perform an extensive study with
 59 the THERMINATOR 2 event generator to account for both non-femtoscopic backgrounds, as well as
 60 contributions from residual correlations induced by feed-down from resonances. We find that the non-
 61 femtoscopic background is due almost entirely to collective effects, and we are able to use the event
 62 generator to quantitatively describe it with unprecedented precision. In the experimental data, we observe
 63 a striking difference between the ΛK^+ and ΛK^- correlations in pairs with low relative momenta ($k^* \lesssim$
 64 100 MeV). The ΛK^+ system exhibits a negative real component of the scattering parameter ($\Re f_0$), while
 65 that of the ΛK^- is positive. The underlying cause dictating this interesting difference in the strong force
 66 between the two systems is not completely understood. The results might suggest an effect arising from
 67 different quark-antiquark interactions between the pairs ($s\bar{s}$ in ΛK^+ and $u\bar{u}$ in ΛK^-), or from different net
 68 strangeness for each system ($S = 0$ for ΛK^+ , and $S = -2$ for ΛK^-). Finally, we find that the ΛK systems
 69 exhibit source radii larger than expected from extrapolation from identical particle femtoscopic studies.
 70 We understand this effect to be result from the separation in space-time of the single-particle Λ and K
 71 distributions. For the study of ΛK pairs at mid-rapidity in Pb-Pb collisions, we expect a separation of the
 72 single-particle sources in the out direction. The effect of a non-zero shift in the source will naturally lead
 73 to larger measured radii.

- 74 Note, we expect and observe consistent results between a particle pair and its conjugate (e.g. ΛK^+ and
 75 $\bar{\Lambda} K^-$); therefore, we group the two together as a single analysis by fitting them simultaneously with
 76 a shared parameter set, and will refer to the joined analysis simply by the pair name, excluding the
 77 conjugate. So, for instance, $\Lambda K_S^0 \oplus \bar{\Lambda} K_S^0$ is simply ΛK_S^0 , $\Lambda K^+ \oplus \bar{\Lambda} K^-$ is ΛK^+ , etc.
- 78 The organization of this paper is as follows. In Sec. 2 we discuss briefly our methods for selecting the
 79 data. In Sec. 3 we present our analysis technique. We introduce the two particle correlation function, as
 80 well as the theoretical models with which we fit. This section also includes descriptions of our handling
 81 of residual correlations, corrections accounting for finite track momentum resolution, treatment of the
 82 non-femtoscopic background, as well as a brief description of our systematic uncertainties estimation.
 83 Our results are presented in Sec. 4, and concluding remarks are given in Sec. 5.

84 2 Data Analysis

85 The dataset analyzed is from Pb-Pb collisions at $\sqrt{s_{NN}} = 2.76$ TeV at the LHC measured by the ALICE
 86 detector [6] in 2011. Approximately 40 million combined central, semi-central, and minimum bias events
 87 were analyzed. The events were classified according to their centrality determined using the measured
 88 amplitudes in the V0 detectors [7]. In order for an event to be included in the analysis, the z-position of
 89 the reconstructed event vertex must be within 10 cm of the center of the ALICE detector, and the event
 90 must contain at least one particle of each type from the pair of interest (e.g. for ΛK_S^0 analysis, an accepted
 91 event must contain at least one Λ and at least one K_S^0).

92 Charged particle tracking was performed using the Time Projection Chamber (TPC) [8] and the Inner
 93 Tracking System [6]. The ITS allows for high spatial resolution in determining the primary (collision)
 94 vertex. The determination of the momenta of the tracks was performed using tracks reconstructed with
 95 the TPC only and constrained to the primary vertex. A minimum requirement of 80 reconstructed TPC
 96 clusters was imposed, the purpose of which is to ensure both the quality of the track and good p_T resolu-
 97 tion at large momenta, as well as to remove fake tracks.

98 Particle identification (PID) for reconstructed tracks was carried out using both the TPC and Time-of-
 99 Flight (TOF) detector [9, 10] in the pseudorapidity range $|\eta| < 0.8$. For TPC PID, a parametrized
 100 Bethe-Bloch formula was used to calculate the specific energy loss $\langle dE/dx \rangle$ in the detector expected
 101 for a particle with a given mass and momentum. For TOF PID, the particle mass was used to calculate
 102 the expected time-of-flight as a function of track length and momentum. For each PID method, a value
 103 ($N\sigma$) was assigned to each track denoting the number of standard deviations between the measured track
 104 information and calculated values. This procedure was repeated for four “particle species hypotheses”
 105 - electron, pion, kaon, and proton-, and, for each hypothesis, a different $N\sigma$ value was obtained per
 106 detector.

107 2.1 K^\pm selection

108 The single-particle selection criteria used to select charged kaon candidates are summarized in Table 1.
 109 K^\pm track detection utilized both TPC and TOF detectors, and tracks within the range $0.14 < p_T < 1.5$
 110 GeV/c were accepted. As we are interested in primary particles originating from the primary vertex,
 111 to reduce the number of secondaries (for instance, charged particles produced in the detector material,
 112 particles from weak decays, etc.) in our sample, we established a maximum cut on the distance-of-
 113 closest-approach (DCA) of the track to the primary vertex. This restriction is realized by imposing a
 114 DCA cut in both the transverse and beam directions.

115 PID was performed using both the TPC and TOF detectors via the $N\sigma$ method. Additionally, we include
 116 methods to reduce the contamination in our K^\pm samples from electrons and pions. The specifics for these
 117 cuts are contained in Table 1.

K[±] selection	
Transverse momentum p_T	$0.14 < p_T < 1.5 \text{ GeV}/c$
$ \eta $	< 0.8
Transverse DCA to primary vertex	$< 2.4 \text{ cm}$
Longitudinal DCA to primary vertex	$< 3.0 \text{ cm}$
TPC and TOF N σ Cuts	
$p < 0.4 \text{ GeV}/c$	$N_{\sigma K, \text{TPC}} < 2$
$0.4 < p < 0.45 \text{ GeV}/c$	$N_{\sigma K, \text{TPC}} < 1$
$0.45 < p < 0.80 \text{ GeV}/c$	$N_{\sigma K, \text{TPC}} < 3$ $N_{\sigma K, \text{TOF}} < 2$
$0.80 < p < 1.0 \text{ GeV}/c$	$N_{\sigma K, \text{TPC}} < 3$ $N_{\sigma K, \text{TOF}} < 1.5$
$p > 1.0 \text{ GeV}/c$	$N_{\sigma K, \text{TPC}} < 3$ $N_{\sigma K, \text{TOF}} < 1$
Electron Rejection: Reject if all satisfied	$N_{\sigma e^-, \text{TPC}} < 3$ $N_{\sigma e^-, \text{TPC}} < N_{\sigma K^\pm, \text{TPC}}$ $N_{\sigma e^-, \text{TOF}} < N_{\sigma K^\pm, \text{TOF}}$
Pion Rejection: Reject if:	
	TOF and TPC available
$p < 0.65 \text{ GeV}/c$	$N_{\sigma \pi, \text{TPC}} < 3$ $N_{\sigma \pi, \text{TOF}} < 3$
	Only TPC available
	$p < 0.5 \text{ GeV}/c$
	$N_{\sigma \pi, \text{TPC}} < 3$
	$0.5 < p < 0.65 \text{ GeV}/c$
	$N_{\sigma \pi, \text{TPC}} < 2$
$0.65 < p < 1.5 \text{ GeV}/c$	$N_{\sigma \pi, \text{TPC}} < 5$ $N_{\sigma \pi, \text{TOF}} < 3$
$p > 1.5 \text{ GeV}/c$	$N_{\sigma \pi, \text{TPC}} < 5$ $N_{\sigma \pi, \text{TOF}} < 2$

Table 1: K[±] selection

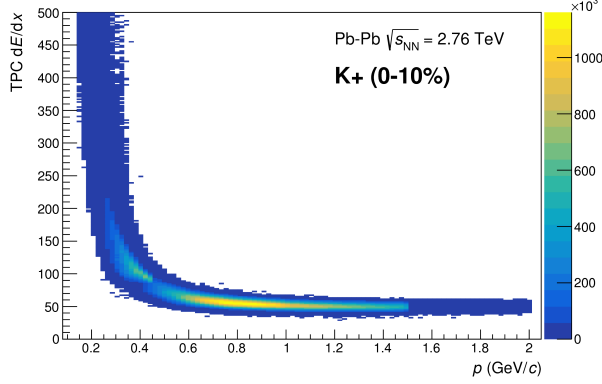


Fig. 1: Sample dE/dx distribution for the K^+ collection from our 0-10% central ΛK^+ analysis.

118 The purity of the K^\pm collections was estimated from a Monte-Carlo (MC) study based on HIJING [11]
 119 simulations using GEANT3 [12] to model particle transport through the ALICE detectors. The charged
 120 kaon purity is estimated to be approximately 97%. Figure 1 shows a sample dE/dx for the K^+ collection
 121 in the 0-10% centrality bin (from our ΛK^+ study).

122 2.2 V^0 selection

123 $\Lambda(\bar{\Lambda})$ and K_S^0 particles are electrically neutral, and cannot be directly detected, but must instead be re-
 124 constructed through detection of their decay products, or daughters. This process is illustrated in Figure
 125 2, and the main cuts used are shown in Tables 2 and 3. In general, particles which are topologically
 126 reconstructed in this fashion are called V^0 particles. The decay channel $\Lambda \rightarrow p\pi^-$ was used for the iden-
 127 tification of Λ hyperons (and, similarly the charge-conjugate decay for the $\bar{\Lambda}$ identification), and $K_S^0 \rightarrow$
 128 $\pi^+\pi^-$ for the identification of K_S^0 mesons.

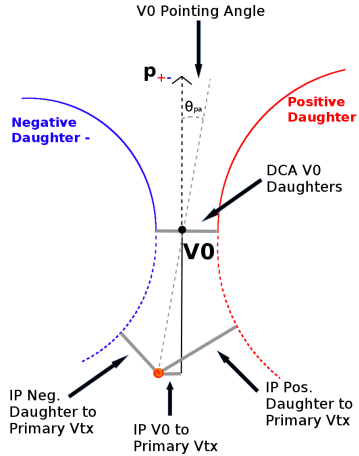


Fig. 2: V^0 Reconstruction

129 To construct a V^0 particle, the charged daughter tracks must first be found. Aside from typical kinematic
 130 and PID cuts (using TPC and TOF detectors), the daughter tracks are also exposed to a minimum cut
 131 on their impact parameter with respect to the primary vertex. The decay vertex of the V^0 is assumed to
 132 be the point of closest approach between the daughter tracks. To help ensure quality, a maximum value
 133 cut is demanded on the distance-of-closest-approach between the daughters (DCA V^0 Daughters). The
 134 positive and negative daughter tracks are combined to form the V^0 candidate, the momentum of which is
 135 simply the sum of the momenta of the daughters (calculated at the DCA).

136 A minimum transverse momentum cut on the V^0 candidate is introduced to reduce contamination from

¹³⁷ fake candidates. Opposite to that of the daughter tracks, the V^0 candidate is exposed to a maximum cut
¹³⁸ on its impact parameter with respect to the primary vertex. In this case, we do want our V^0 candidates
¹³⁹ to be primary, hence the maximum cut imposition. To further strengthen our selection of primary V^0
¹⁴⁰ candidates, we impose a selection on the pointing angle, θ_{pa} , between the V^0 momentum and the vector
¹⁴¹ pointing from the primary vertex to the secondary V^0 decay vertex, which is achieved by appointing a
¹⁴² minimum value on $\cos(\theta_{pa})$ (“Cosine of pointing angle” in Tables 2 and 3).

¹⁴³ On occasion, $\Lambda(\bar{\Lambda})$ particles are misidentified as K_S^0 , and vice versa. To attempt to remove these contam-
¹⁴⁴inations without throwing away good candidates, we impose a set of misidentification cuts. The intent
¹⁴⁵of these cuts is to judge whether a candidate is more likely a $\Lambda(\bar{\Lambda})$ or a K_S^0 , and are implemented as
¹⁴⁶described below. For a given V^0 , we calculate the mass assuming different identities (Λ , $\bar{\Lambda}$, K_S^0) of the
¹⁴⁷candidate; the mass assuming K_S^0 hypothesis ($m_{inv, K_S^0 \text{ hyp.}}$) is calculated assuming $\pi^+\pi^-$ daughters, the
¹⁴⁸mass assuming Λ hypothesis ($m_{inv, \Lambda \text{ hyp.}}$) is calculated assuming $p\pi^-$ daughters, and the mass assum-
¹⁴⁹ing $\bar{\Lambda}$ hypothesis ($m_{inv, \bar{\Lambda} \text{ hyp.}}$) is calculated assuming $\bar{p}\pi^+$ daughters. In addition to the notation just
¹⁵⁰introduced, in the following, m_{PDG, K_S^0} and $m_{PDG, \Lambda(\bar{\Lambda})}$ denote the particle masses of the K_S^0 and $\Lambda(\bar{\Lambda})$,
¹⁵¹respectively, as recorded by the Particle Data Group [13].

¹⁵² For $\Lambda(\bar{\Lambda})$ selection, a candidate is assumed to be misidentified and is rejected if all of the following
¹⁵³criteria are satisfied:

- ¹⁵⁴ 1. $|m_{inv, K_S^0 \text{ hyp.}} - m_{PDG, K_S^0}| < 9.0 \text{ MeV}/c^2$
- ¹⁵⁵ 2. The daughter particles pass daughter cuts intended for K_S^0 reconstruction
- ¹⁵⁶ 3. $|m_{inv, K_S^0 \text{ hyp.}} - m_{PDG, K_S^0}| < |m_{inv, \Lambda(\bar{\Lambda}) \text{ hyp.}} - m_{PDG, \Lambda(\bar{\Lambda})}|$

¹⁵⁷ Similarly, for K_S^0 selection, a candidate is rejected if all of the following criteria are satisfied for the Λ
¹⁵⁸case, or for the $\bar{\Lambda}$ case:

- ¹⁵⁹ 1. $|m_{inv, \Lambda(\bar{\Lambda}) \text{ hyp.}} - m_{PDG, \Lambda(\bar{\Lambda})}| < 9.0 \text{ MeV}/c^2$
- ¹⁶⁰ 2. The daughter particles pass daughter cuts intended for $\Lambda(\bar{\Lambda})$ reconstruction
- ¹⁶¹ 3. $|m_{inv, \Lambda(\bar{\Lambda}) \text{ hyp.}} - m_{PDG, \Lambda(\bar{\Lambda})}| < |m_{inv, K_S^0 \text{ hyp.}} - m_{PDG, K_S^0}|$

¹⁶² At this stage, we have a collection of V^0 candidates satisfying all of the aforementioned cuts. However,
¹⁶³ this collection is still polluted by fake V^0 's, for which the daughter particles happen to pass all of our cuts,
¹⁶⁴but which do not actually originate from a V^0 . Although the two daughter particles appear to reconstruct
¹⁶⁵a V^0 candidate, they are lacking one critical requirement: the system invariant mass does not match that
¹⁶⁶of our desired V^0 species (these can be seen outside of the mass peaks in Fig. 3). Therefore, as our final
¹⁶⁷single-particle cut, we require the invariant mass of the V^0 candidate to fall within the mass peak of our
¹⁶⁸desired species. Note, however, that some fake V^0 's still make it past this final cut, as their invariant mass
¹⁶⁹also happens to fall without our acceptance window.

¹⁷⁰ Occasionally, we encounter a situation where two V^0 candidates share a common daughter. Not both of
¹⁷¹these candidates can be real V^0 's, and including both could introduce an artificial signal into our data.
¹⁷² To avoid any auto-correlation effects, for each event, we impose a single-particle shared daughter cut on
¹⁷³each collection of V^0 candidates. This cut iterates through the V^0 collection to ensure that no daughter is
¹⁷⁴claimed by more than one V^0 candidate. If a shared daughter is found between two V^0 candidates, that
¹⁷⁵candidate with a smaller DCA to primary vertex is kept while the other is excluded from the analysis.

Λ selection	
Transverse momentum p_T	> 0.4 GeV/c
$ \eta $	< 0.8
$ m_{\text{inv}} - m_{\text{PDG}} $	< 3.8 MeV
DCA to primary vertex	< 0.5 cm
Cosine of pointing angle	> 0.9993
Decay Length	< 60 cm
Daughter Cuts (π and p)	
$ \eta $	< 0.8
DCA πp Daughters	< 0.4 cm
π-specific cuts	
p_T	> 0.16 GeV/c
DCA to primary vertex	> 0.3 cm
TPC and TOF N σ Cuts	
$p < 0.5 \text{ GeV}/c$	N $\sigma_{\text{TPC}} < 3$
$p > 0.5 \text{ GeV}/c$	TOF & TPC available N $\sigma_{\text{TPC}} < 3$ N $\sigma_{\text{TOF}} < 3$
	Only TPC available N $\sigma_{\text{TPC}} < 3$
p-specific cuts	
p_T	> 0.5(p) [0.3(\bar{p})] GeV/c
DCA to primary vertex	> 0.1 cm
TPC and TOF N σ Cuts	
$p < 0.8 \text{ GeV}/c$	N $\sigma_{\text{TPC}} < 3$
$p > 0.8 \text{ GeV}/c$	TOF & TPC available N $\sigma_{\text{TPC}} < 3$ N $\sigma_{\text{TOF}} < 3$
	Only TPC available N $\sigma_{\text{TPC}} < 3$

Table 2: Λ selection

K_S⁰ selection	
Transverse momentum p_T	> 0.2 GeV/c
$ \eta $	< 0.8
$m_{\text{PDG}} - 13.677 \text{ MeV} < m_{\text{inv}} < m_{\text{PDG}} + 2.0323 \text{ MeV}$	
DCA to primary vertex	< 0.3 cm
Cosine of pointing angle	> 0.9993
Decay Length	< 30 cm
π^{\pm} Daughter Cuts	
p_T	> 0.15 GeV/c
$ \eta $	< 0.8
DCA $\pi^+ \pi^-$ Daughters	< 0.3 cm
DCA to primary vertex	> 0.3 cm
TPC and TOF N σ Cuts	
$p < 0.5 \text{ GeV}/c$	N $\sigma_{\text{TPC}} < 3$
$p > 0.5 \text{ GeV}/c$	TOF & TPC available N $\sigma_{\text{TPC}} < 3$ N $\sigma_{\text{TOF}} < 3$
	Only TPC available N $\sigma_{\text{TPC}} < 3$

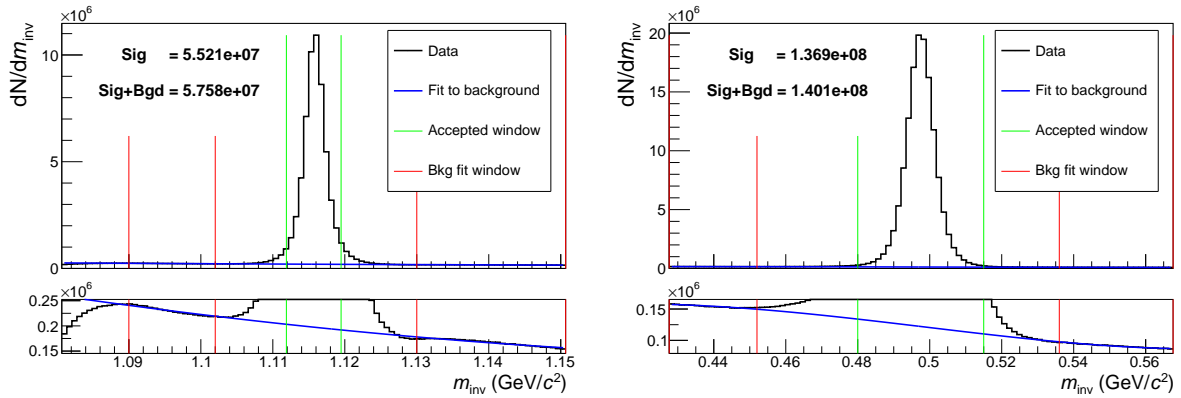
Table 3: K_S⁰ selection

176 Note, this single-particle shared daughter cut is unique from the pair shared daughter cut discussed in
 177 Sec. 2.3, the latter of which ensure there is no daughter sharing between the particles in a given pair.

178 In order to obtain a true and reliable signal, one must ensure good purity of the V^0 collection. The purity
 179 of the collection is calculated as:

$$\text{Purity} = \frac{\text{Signal}}{\text{Signal} + \text{Background}} \quad (1)$$

180 To access both the signal and background, the invariant mass distribution (m_{inv}) of all V^0 candidates
 181 must be constructed immediately before the final invariant mass cut, as shown in Fig. 3 for Λ and K_S^0
 182 candidates in the 0-10% centrality bin. Figure 3(a) presents the $p\pi^-$ invariant mass distribution showing
 183 the Λ peak, and Figure 3(b) presents the $\pi^+\pi^-$ invariant mass distribution showing the K_S^0 peak. These
 184 distributions (and similar for $\bar{\Lambda}$) are used to calculate the collections' purities (defined in Eq. 1). As
 185 shown in Figure 3, the background is fit (with a polynomial) outside of the peak region of interest to
 186 obtain an estimate for the background within the region. Within the m_{inv} cut limits, the background is
 187 assumed to be the region below the fit while the signal is that above the fit. The Λ and $\bar{\Lambda}$ purities were
 188 found to be $\approx 95\%$, and the K_S^0 purity was found to be $\approx 98\%$.



(a) $p\pi^-$ invariant mass distribution where the Λ peak is seen. (b) $\pi^+\pi^-$ invariant mass distribution where the K_S^0 peak is seen.

Fig. 3: Invariant mass (m_{inv}) distribution of $p\pi^+$ pairs showing the Λ peak 3(a), and of $\pi^+\pi^-$ pairs showing the K_S^0 peak 3(b), for V^0 candidates. The bottom panels are zoomed to show the background with fit. The vertical green lines represent the m_{inv} cuts used in the analyses, the red vertical lines delineate the region over which the background was fit, and the blue line shows the background fit.

189 2.3 Pair Construction

190 In order to reduce the contamination to the two-particle correlations due to split or merged tracks and
 191 pairs sharing daughters, two main pair cuts are applied: a shared daughter cut, and an average separation
 192 cut. The purpose of the shared daughter cut is to ensure the first particle in the pair is unique from the
 193 second. For pairs formed of two V^0 s (i.e. ΛK_S^0), this cut is implemented by removing all pairs which
 194 share a daughter. For a pair formed of a single V^0 and a charged track (i.e. ΛK^\pm), the cut removes all
 195 pairs in which the charged track is also claimed as a daughter of the V^0 .

196 The purpose of the average separation cut is to remove splitting and merging effects, and it is employed
 197 in the following way. To calculate the average separation between two tracks, the spatial separation is
 198 determined at several points throughout the TPC (every 20 cm radially from 85 cm to 245 cm), and the
 199 results averaged. For that ΛK_S^0 analysis, which involves two V^0 particles, a minimum average separation
 200 cut of 6 cm between the like-charge daughters in the pairs was imposed (for example, between the p

daughter of the Λ and the π^+ daughter of the K_S^0). For the ΛK^\pm analyses, a minimum average separation cut of 8 cm was enforced between the K^\pm and the Λ daughter sharing the same charge (for example, in the ΛK^+ analysis, between the p daughter of the Λ and the K^+). The values used in these cuts were obtained by first forming average separation correlation functions. This is done just as for our relative-momentum correlation functions, but we instead bin in average separation. Looking at these average separation correlation functions for like-charge tracks, at lowest average separation we see an enhancement due to track splitting, followed by (at slightly higher average separation) a suppression due to track merging. When the average separation correlation function stabilizes to unity, these effects are no longer abundant, and we choose our cut value. Splitting and merging effects between oppositely charged tracks was found to be negligible, therefore no cuts on unlike-charge tracks were imposed.

3 Analysis Methods

3.1 Correlation Function

Two-particle correlation functions are built as the ratio of the covariant two-particle and single-particle spectra:

$$C^{ab}(\vec{p}_a, \vec{p}_b) = \frac{E_a E_b \frac{dN^{ab}}{d^3 p_a d^3 p_b}}{(E_a \frac{dN^a}{d^3 p_a})(E_b \frac{dN^b}{d^3 p_b})} \quad (2)$$

This may be expressed theoretically as in the Koonin-Pratt equation [14, 15]:

$$C(\mathbf{k}^*) = \int S_{\mathbf{P}}(\mathbf{r}^*) |\Psi_{\mathbf{k}^*}(\mathbf{r}^*)|^2 d^3 \mathbf{r}^* \quad (3)$$

where \mathbf{k}^* is the relative momentum of the pair (defined as $\mathbf{k}^* = \frac{1}{2}|\mathbf{p}_1^* - \mathbf{p}_2^*|$, where \mathbf{p}_1^* and \mathbf{p}_2^* are the momenta of the two particles) in the pair rest frame (PRF), \mathbf{r}^* is the relative separation in the same frame, \mathbf{P} is the total pair momentum, $S_{\mathbf{P}}(\mathbf{r}^*)$ is the pair source distribution, and $\Psi_{\mathbf{k}^*}(\mathbf{r}^*)$ is the two-particle wave-function. Within the $|\Psi|^2$ term is contained the particle interaction information, and therefore the scattering parameters. Equation 3 reveals the limitations of femtoscopy; at best, we are able to probe the distribution of relative positions of particles with identical velocities and total momentum \mathbf{P} as they move in an asymptotic state. Therefore, we do not measure the entire size of the source, but rather the “regions of homogeneity” [3].

In practice, the correlation function is formed experimentally as:

$$C(k^*) = \mathcal{N} \frac{A(k^*)}{B(k^*)} \quad (4)$$

where $A(k^*)$ is the signal distribution, $B(k^*)$ is the reference distribution, and \mathcal{N} is a normalization parameter. $B(k^*)$ is used to divide out the phase-space effects, leaving only the femtoscopic effects in the correlation function. The normalization parameter is chosen such that the mean value of the correlation function equals unity for $k^* \in [0.32, 0.4] \text{ GeV}/c$.

In practice, $A(k^*)$ is constructed by binning in k^* pairs from the same event. Typically, $B(k^*)$ is obtained by forming mixed-event pairs, i.e. particles from a given event are paired with particles from N_{mix} other events, and these pairs are then binned in k^* . Other techniques exist; most notably, one may use same-event pairs after rotating one particle in the pair by 180° in the transverse plane (see Sec. 3.5 and App. B for more details). However, for this analysis, we use the typical mixed-event method. In order to mix only similar events, we bin our events both in primary vertex location (2 cm bin width) and in centrality

(5% bin width), and we only mix events within a given bin; i.e. we only mix events of like centrality and of like primary vertex location. Additionally, we use $N_{\text{mix}} = 5$ as the size of our mixing pool. Also note, a vertex correction is also applied to each event, which essentially recenters the the primary vertices to $z = 0$.

This analysis presents correlation functions for three centrality bins (0-10%, 10-30%, and 30-50%), and is currently pair transverse momentum ($k_T = \frac{1}{2}|\mathbf{p}_{T,1} + \mathbf{p}_{T,2}|$) integrated (i.e. not binned in k_T). The correlation functions are constructed separately for the two magnetic field configurations (++ and --). These are kept separate during the fitting process, and are combined using a weighted average when plotting, where the weight is the number of numerator pairs in the normalization range.

3.2 Modeling the correlation function

In the absence of the Coulomb interaction, the correlation function can be described analytically with a model derived by Lednický and Lyuboshitz [5]. Within the model, the (non-symmetrized) two-particle wave function is expressed as a superposition of a plane wave and diverging spherical wave:

$$\Psi^S(\mathbf{k}^*, \mathbf{r}^*) = e^{-i\mathbf{k}^* \cdot \mathbf{r}^*} + f^S(k^*) \frac{e^{ik^* r^*}}{r^*} \quad (5)$$

In the effective range approximation, the complex s-wave scattering amplitude, $f^S(k^*)$, with S denoting the total spin of the particular pair, is of the form

$$f^S(k^*) = \left(\frac{1}{f_0^S} + \frac{1}{2} d_0^S k^{*2} - ik^* \right)^{-1} \quad (6)$$

where f_0^S is the complex s-wave scattering length, and d_0^S is the effective range of the interaction. A spherically symmetric Gaussian distribution with radius R_{inv} is assumed for the pair emission source in the PRF. Assuming unpolarized emission, using the appropriately symmetrized form of Ψ (Eq. 5) with a spherically symmetric Gaussian source (Eq. ??), with the Koonin-Pratt equation (Eq. 3), the correlation function for uncharged particles is given by [5]

$$C(k^*) = 1 + C_{\text{QI}}(k^*) + C_{\text{FSI}}(k^*) \quad (7)$$

C_{QI} describes plane-wave quantum interference:

$$C_{\text{QI}}(k^*) = \alpha \exp(-4k^{*2}R^2) \quad (8)$$

where $\alpha = (-1)^{2j}/(2j+1)$ for identical particles with spin j , and $\alpha = 0$ for non-identical particles. C_{FSI} describes the s-wave strong final state interaction between the particles:

$$C_{\text{FSI}}(k^*) = \sum_S \rho_S \left[\frac{1}{2} \left| \frac{f^S(k^*)}{R_{\text{inv}}} \right|^2 \left(1 - \frac{d_0^S}{2\sqrt{\pi}R_{\text{inv}}} \right) + \frac{2\Re f^S(k^*)}{\sqrt{\pi}R_{\text{inv}}} F_1(2k^* R_{\text{inv}}) - \frac{\Im f^S(k^*)}{R_{\text{inv}}} F_2(2k^* R_{\text{inv}}) \right] \quad (9)$$

where

$$F_1(z) = \int_0^z \frac{e^{x^2-z^2}}{z} dx; \quad F_2(z) = \frac{1-e^{-z^2}}{z} \quad (10)$$

259 The weight factor, ρ_S is the normalized emission probability for a state of total spin S ; in the assumed
 260 case of unpolarized emission, $\rho_S = (2S+1)/[(2j_1+1)(2j_2+1)]$, where $j_{1,2}$ are the spins of the particles
 261 in the pair.

262 An additional parameter λ is typically included in the femtoscopic fit function to account for the purity of
 263 the pair sample, as well as the presence of any uncorrelated pairs. In the case of no residual correlations
 264 (to be discussed in Section 3.3), the fit function becomes:

$$C(k^*) = 1 + \lambda [C_{\text{QI}}(k^*) + C_{\text{FSI}}(k^*)] \quad (11)$$

265 The presented formalism simplifies for the ΛK system. The particles in the pairs are obviously non-
 266 identical, therefore $\alpha = 0$, and we need not worry about the quantum statistical term, C_{QI} . Furthermore,
 267 Λ is spin-1/2 and K are spin-0, so the ΛK system only has one possible total spin state S , and therefore
 268 C_{FSI} has only a single term. In the following, we drop the S superscript from all scattering parameters.

269 3.3 Residual Correlations

270 The purpose of this analysis is study the interaction and scale of the emitting source of the primary
 271 ΛK pairs. In order to obtain correct results, it is desirable for our particle collections to consist of
 272 primary particles. In practice, this is impossible to achieve; many of our particles are not primary,
 273 but originate as decay products from other resonances. Some of our Λ hyperons decay from Σ^0 , Ξ^0 ,
 274 Ξ^- and $\Sigma^{*(+, -, 0)}(1385)$ parents, and some of our K mesons decay from $K^{*(+, -, 0)}(892)$ parents. In
 275 these decays, the daughter carries away a momentum very similar to that of its parent. As a result,
 276 the correlations between the particles in the daughter pair will be sensitive to, and dependent upon, the
 277 interaction between the parents. In effect, the correlation between the parents will be visible, although
 278 smeared out, in the daughters' signal. We call this a residual correlation resulting from feed-down.

279 The finally measured correlation function is a combination of the genuine ΛK correlation with contribu-
 280 tions from residual feed-down and misidentified particles

$$\begin{aligned} C_{\text{measured}}(k_{\Lambda K}^*) &= 1 + \lambda'_{\Lambda K}[C_{\Lambda K}(k_{\Lambda K}^*) - 1] + \sum_{i,j} \lambda'_{ij}[C_{ij}(k_{\Lambda K}^*) - 1] \\ \lambda'_{ij} &= \lambda_{\text{Fit}} \lambda_{ij} \\ \sum_{i,j} \lambda'_{ij} &= \lambda_{\text{Fit}} \sum_{i,j} \lambda_{ij} = \lambda_{\text{Fit}} \end{aligned} \quad (12)$$

281 where the ΛK term represents the genuine ΛK correlation, and the i, j terms denote the contributions
 282 from residual feed-down and possible impurities. More specifically, $C_{ij}(k_{\Lambda K}^*)$ is the correlation function
 283 between parents of particle species i and j , expressed in the basis of the relative momentum of the
 284 observed daughter ΛK pairs. The λ parameters serve as weight dictating the strength of the parent
 285 contribution to the daughter pair, and are normalized to unity. The individual λ_{ij} are fixed (and whose
 286 values can be found in Table A.1), but the parameter λ_{Fit} is left free. The λ_{Fit} parameter serves as an
 287 overall normalization shared by all contributors.

288 In order to obtain the parent correlation function expressed in the relative momentum of the daughter
 289 pair, one must use a transform matrix. The transform matrix describes the decay kinematics of the parent
 290 system into the daughter, and maps the k^* of the parent pair onto that of the daughter. Using this matrix,
 291 the transformed residual correlation function can be obtained:

$$C_{ij}(k_{\Lambda K}^*) \equiv \frac{\sum_{k_{ij}^*} C_{ij}(k_{ij}^*) T(k_{ij}^*, k_{\Lambda K}^*)}{\sum_{k_{ij}^*} T(k_{ij}^*, k_{\Lambda K}^*)} \quad (13)$$

292 The transform matrix is generated with the THERMINATOR 2 [17] simulation. It is formed for a given
 293 parent pair, ij , by taking all ΛK pairs originating from ij , calculating the relative momentum of the
 294 parents (k_{ij}^*) and daughters ($k_{\Lambda K}^*$), and filling a two-dimensional histogram with the values. The transform
 295 matrix is essentially an unnormalized probability distribution mapping the k^* of the parent pair to that of
 296 the daughter pair when one or both parents decay.

297 Femtoscopic analyses are sensitive to the pair emission structure at kinetic freeze-out. Therefore, in the
 298 eyes of femtoscopy, any particle born from a resonance decay before last rescattering is seen as primary.
 299 For our study, when including three residual contributors, we consider a particle to be primary if its
 300 parent has a proper decay length of $c\tau < 10$ fm. When including ten residual contributors, we must
 301 reduce this number to $c\tau < 4$ fm for consistency. Moving to ten contributors, we introduce feed-down
 302 from Σ^* and K^* resonances, with proper decay lengths of $c\tau \approx 5$ fm and $c\tau \approx 4$ fm, respectively. As
 303 these are considered non-primary for the case of ten contributors, so must any resonance with $c\tau > 4$ fm.
 304 As previously stated, the λ parameters dictate the strength of the parent contribution to the daughter pair.
 305 Therefore, the λ parameter for parent system AB can be estimated as the total number of ΛK pairs in our
 306 experimental sample originating from AB (N_{AB}) divided by the total number of ΛK pairs (N_{Total}):

$$\lambda_{AB} = \frac{N_{AB}}{N_{Total}} \quad (14)$$

307 The particle yields can be estimated using THERMINATOR 2 simulation (N_{ij}^{THERM}), while the reconstruc-
 308 tion efficiencies (RE_{ij}) are estimated with MC HIJING data, which has been run through GEANT to
 309 simulate the detector response. Thus, the λ parameters are estimated as:

$$\lambda_{AB} = \frac{N_{AB}}{N_{Total}} = \frac{N_{AB}^{THERM} RE_{AB}^{HIJING}}{\sum_{ij} N_{ij}^{THERM} RE_{ij}^{HIJING}} \quad (15)$$

310 The λ values used can be found in Table A.1, for the case of both three and ten residual contributors. In
 311 the table, we also list the λ values used for “Other” and “Fakes”. The “Other” category contains pairs
 312 which are not primary, and which do not originate from the (3 or 10) residual pairs included in the fit. The
 313 “Fakes” category represents pairs that are mistakenly identified as ΛK. To estimate this λ_{Fakes} value, we
 314 assumed that the number of fake pairs was equal to the total number of pairs multiplied by the Λ purity
 315 (i.e. assuming perfect purity for the kaons); or, more simply, $\lambda_{Fakes} = 1.0 - \text{Purity}(\Lambda)$. For both of these
 316 contributors (“Other” and “Fakes”), we assume that these correlations average to unity, and therefore do
 317 not contribute to the final correlation function.

318 In practice, we model the correlation function of the parents (e.g. $\Sigma^0 K^+$), and run the correlation func-
 319 tion through the appropriate transform matrix to determine the contribution to the daughter correlation
 320 function (e.g. ΛK^+). In an ideal world, we would simply look up the parent interaction in some table,
 321 and input this into our model, and form the parent correlation function, C_{ij} . Unfortunately, the world
 322 in which we live is not perfect, such a table does not exist, and little is known about the interaction be-
 323 tween the particles in the residual pairs of this study. Additionally, introducing a unique set of scattering
 324 parameters and radii for each residual system would introduce a large number of additional fit parame-
 325 ters, for which we do not have many constraints, and would cause our fitter to be too unconstrained and

yield untrustworthy results. For this analysis, we assume all residual pairs have the same source size as the daughter pair. Furthermore, we assume Coulomb-neutral residual pairs share the same scattering parameters as the daughter pair. Therefore, for Coulomb-neutral pairs, such as $\Sigma^0 K$, and $\Xi^0 K$, $C_{ij}(k_{ij}^*)$ is calculated from Eqn. 7, with the help of Eqn. 9; $C_{ij}(k_{\Lambda K}^*)$ is then obtained by transforming $C_{ij}(k_{ij}^*)$ with Eq. 13, using the appropriate transform matrix.

For residual pairs affected by both the strong and Coulomb interactions, things are a bit more complicated. This is due to the fact that, for the case of both strong and Coulomb interaction, we no longer have a nice analytical form with which to fit. Generating a correlation function including both is also time consuming, as described further in Appendix C. When modeling $\Xi^- K^\pm$ residual correlations, we use the experimental $\Xi^- K^\pm$ data; in this case, there is no need to make any assumptions about scattering parameters or source sizes. For the other cases, we assume the strong interaction is negligible, and generate the parent correlation assuming a Coulomb-only scenario (see Appendix C for more details). This approximation is well justified here as a Coulomb-only description of the system describes, reasonably well, the broad features of the correlation; the strong interaction is necessary for the fine details. However, as these correlations are run through a transform matrix, which largely flattens out and fine details, a Coulomb-only description should be sufficient. This is reinforced by the fact that we find consistent results between using the ΞK data and the Coulomb-only model of the ΞK data in our treatment of the residual contribution.

3.4 Momentum Resolution Corrections

Finite track momentum resolution causes the reconstructed momentum of a particle to smear around the true value. This, of course, also holds true for V^0 particles. The effect is propagated up to the pairs of interest, which causes the reconstructed relative momentum (k_{Rec}^*) to differ from the true momentum (k_{True}^*). Smearing of the momentum typically will result in a suppression and broadening of the signal.

The effects of finite momentum resolution can be investigated using the MC data, for which both the true and reconstructed momenta are available. Information gained from looking at k_{Rec}^* vs k_{True}^* can be exploited to generate response matrices. A response matrix describes quantitatively how each k_{Rec}^* bin receives contributions from multiple k_{True}^* bins, and can be used to account for the effects of finite momentum resolution. With this approach, the resolution correction is applied on-the-fly during the fitting process by propagating the theoretical (fit) correlation function through the response matrix, according to:

$$C_{\text{fit}}(k_{\text{Rec}}^*) = \frac{\sum_{k_{\text{True}}^*} M_{k_{\text{Rec}}^*, k_{\text{True}}^*} C_{\text{fit}}(k_{\text{True}}^*)}{\sum_{k_{\text{True}}^*} M_{k_{\text{Rec}}^*, k_{\text{True}}^*}} \quad (16)$$

where $M_{k_{\text{Rec}}^*, k_{\text{True}}^*}$ is the response matrix, $C_{\text{fit}}(k_{\text{True}}^*)$ is the fit binned in k_{True}^* , and the denominator normalizes the result. Equation 16 describes that, for a given k_{Rec}^* bin, the observed value of $C(k_{\text{Rec}}^*)$ is a weighted average of all $C(k_{\text{True}}^*)$ values, where the weights are the normalized number of counts in the $[k_{\text{Rec}}^*, k_{\text{True}}^*]$ bin.

3.5 Non-Flat Background

We observe a significant non-femtoscopic, non-flat, background in all of our correlations at large k^* . This background increases with decreasing centrality, is the same amongst all ΛK^\pm pairs, and is more pronounced in the ΛK_S^0 system. This difference in ΛK^\pm and ΛK_S^0 backgrounds is due mainly to the difference in kinematic cuts, not due to any interesting physics.

It is suggested that this background effect is due primarily to particle collimation associated with elliptic

366 flow [18]. More specifically, these backgrounds result from mixing events with unlike event-plane angles
 367 (Ψ_{EP}). As explained in [18], when elliptic flow is present, all particles are more likely to be emitted in
 368 a specific direction (in-plane), as opposed to a perpendicular direction. Therefore, the difference in
 369 momenta for pairs of particles tends to be smaller, compared to the case of no flow. In the case of mixed-
 370 event pairs, the two events used do not share an event-plane, and therefore there is no collimation effect
 371 in the pairs from flow. As a result, pairs with larger momentum are more likely when mixed-events are
 372 used (in the denominator of the correlation function), causing the correlation function to dip below unity.
 373 This same reasoning suggests that the background should lead to an enhancement at low- k^* .

374 The issue here is that we need to know the behavior of the non-femtoscopic background in the low-
 375 k^* region, but we only cleanly observe it in the region further out where there is no femtoscopic signal.
 376 Unfortunately, we cannot simply rotate each event to artificially align their event-planes and rid ourselves
 377 of this mixing effect, as our azimuthal angle acceptance is not perfectly uniform, and we have only finite
 378 event-plane resolution. With better resolution, one could simply bin events in Ψ_{EP} and only mix events
 379 within a given bin. We pursued this direction, and observed a slight decrease in the background; however,
 380 going to finer binning, we saw no additional reduction in the background, signaling that we had reached
 381 the limits dictated by the resolution. In the end, we are forced to model the background to include it into
 382 our fit.

383 THERMINATOR 2 simulation has been shown to reproduce the background features in a πK analysis
 384 [18]. After issuing each simulated event a random Ψ_{EP} , we found THERMINATOR 2 did an exceptional
 385 job of describing our data. Furthermore, the simulation showed the non-femtoscopic background affects
 386 the correlation function as a separable scale factor. Figure 4 shows the THERMINATOR 2 simulation
 387 (gold) together with experimental data (red, blue, or black). The figure also shows a 6th-order polynomial
 388 fit to the simulation (gold), as well as the fit polynomial scaled to match the data (red, blue, black).

389 The description by THERMINATOR 2 of the non-femtoscopic backgrounds in the ΛK^\pm systems is re-
 390 markable, and can be used in a quantitative fashion to help fit the data. More specifically, the non-
 391 femtoscopic backgrounds were modeled by (6th-)order polynomial fits to THERMINATOR 2 simulation
 392 for the ΛK^\pm analyses; one polynomial for each centrality class. The form of each polynomial was set
 393 before use with the experimental data, by fitting to the THERMINATOR 2 simulation, shown in Fig. 4.
 394 At the time of the fit, the polynomial used to correct each correlation function could only be adjust by a
 395 simple scale factor to best match the data.

396 The description of the ΛK_S^0 is good at a qualitative level, but not quantitatively good enough to be utilized
 397 in our fit. As such, we use a linear form to model the background in the ΛK_S^0 system. The background for
 398 each correlation function was fixed before use in the signal region by fitting a linear form to the region
 399 $0.6 < k^* < 0.9$ GeV/c. In all cases, the non-femtoscopic background correction was applied as a scale
 400 factor.

401 An alternative approach to treating the non-femtoscopic background is to instead attempt to eliminate
 402 it. The background may be effectively reduced by forming the reference distribution ($B(k^*)$) with the
 403 “Stavinskiy method”. With the Stavinskiy method, mixed-event pairs are not used for the reference
 404 distribution; instead, same-event pseudo-pairs, formed by rotating one particle in a real pair by 180°
 405 in the transverse plane, are used. This rotation rids the pairs of any femtoscopic correlation, while
 406 maintaining correlations due to elliptic flow (and other suitably symmetric contributors). The effect on
 407 our ΛK^+ correlation functions can be seen in the appendix, in Fig. B.1.

408 3.6 Summarized Fit Procedure

409 A simple χ^2 test is inappropriate for fitting correlation functions, as the ratio two Poisson distributions
 410 does not result in a Poisson distribution. Instead, a log-likelihood fit function of the following form is
 411 used [1]:

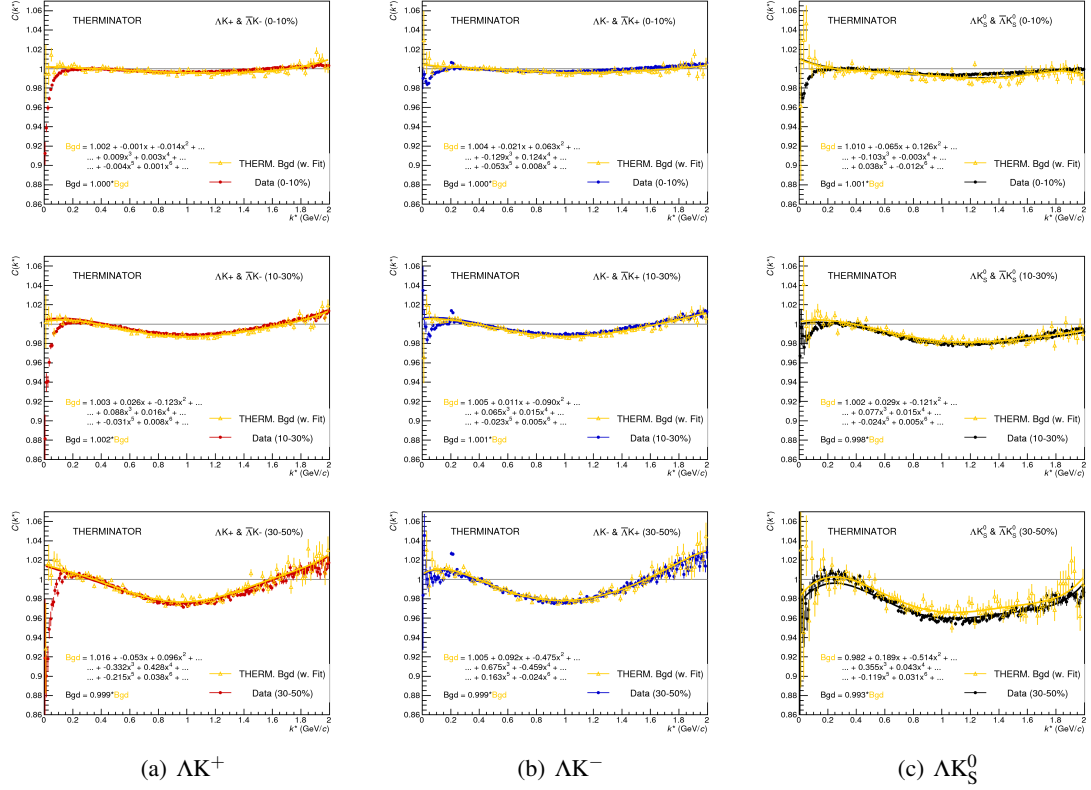


Fig. 4: THERMINATOR 2 simulation (gold) together with experimental data (red, blue, or black). The left column shows results for ΛK^+ (4(a)), middle for ΛK^- (4(b)), and right for ΛK_S^0 (4(c)). A 6th-order polynomial fit to the simulation is shown as a solid gold line, and whose fit parameters are printed on the lower left of each plot. This polynomial is scaled to match the experimental data; the value of this scale is printed in the lower left corner of each plot. The polynomial fit with scale factor applied is drawn in a color matching the experimental data (red, blue, black).

$$\chi_{PML}^2 = -2 \left[A \ln \left(\frac{C(A+B)}{A(C+1)} \right) + B \ln \left(\frac{A+B}{B(C+1)} \right) \right] \quad (17)$$

412 where A is the experimental signal distribution (numerator), B is the experimental reference distribution
 413 (denominator), and C is the theoretical fit correlation function. Therefore, we use Eq. 17 as the statistic
 414 quantifying the quality of the fit. The parameters of the fit are: λ , R , f_0 ($\Re f_0$ and $\Im f_0$ separately), d_0 ,
 415 and normalization N .

416 With our procedure, we are able to share parameters between different analyses and fit all simultaneously.
 417 A given pair and its conjugate (e.g. ΛK^+ and $\bar{\Lambda} K^-$) always share scattering parameters ($\Re f_0$, $\Im f_0$, d_0).
 418 However, the three distinct analyses (ΛK^+ , ΛK^- , and ΛK_S^0) are assumed to have scattering parameters
 419 unique from each other. We assume the pair emission source for a given centrality class is similar between
 420 all analyses; therefore, for each centrality, all ΛK analyses share a common radius parameter. We assume
 421 the same is true for the overall normalization λ parameters in Eq. 13. Finally, each correlation function
 422 has a unique normalization parameter.

423 All correlation functions were normalized in the range $0.32 < k^* < 0.40$ GeV/c, and fit in the range 0.0
 424 $< k^* < 0.30$ GeV/c. For the ΛK^- analysis, the region $0.19 < k^* < 0.23$ GeV/c was excluded from the
 425 fit to exclude the bump caused by the Ω^- resonance. For each pair system, we account for contributions
 426 from three residual contributors, as discussed in Sec. 3.3, and whose individual λ values are listed in

427 Table A.1 (the cases of zero and ten residual contributors were also investigated, but the case of three
 428 contributors was deemed most reasonable). We account for effects of finite track momentum resolution,
 429 as outlined in Sec. 3.4. The non-femtoscopic backgrounds are modeled using the THERMINATOR 2
 430 simulation for the ΛK^\pm analyses, and with a linear form for the ΛK_S^0 system, as described in Sec. 3.5. In
 431 general, corrections are applied to the fit function, the raw data is never touched.

432 To summarize, the complete fit function is constructed as follows:

- 433 1. The uncorrected, primary, correlation function, $C_{\Lambda K}(k_{\text{True}}^*)$, is constructed using Eqns. 7 and 9
- 434 2. The correlation functions describing the parent systems which contribute residually are obtained
 435 using:
 - 436 – Eqns. 7 and 9 for the case of Coulomb-neutral pairs
 - 437 – $\Xi^- K^\pm$ experimental data for $\Xi^- K^\pm$ contributions
 - 438 – a Coulomb-only curve, with the help of Appendix C, for other pairs including the Coulomb
 439 interaction
- 440 3. The residual contributions to the ΛK correlation function is found by running each parent correla-
 441 tion function through the appropriate transform matrix, via Eq. 13
- 442 4. The primary and residual correlations are combined, via Eq. 12 with Tab. A.1, to form $C'_{Fit}(k_{\text{True}}^*)$
- 443 5. The correlation function is corrected to account for momentum resolution effects using Eq. 16, to
 444 obtain $C'_{Fit}(k_{\text{Rec}}^*)$
- 445 6. Finally, the non-flat background correction, $F_{\text{Bgd}}(k_{\text{Rec}}^*)$ is applied, and the final fit function is ob-
 446 tained, $C_{\text{Fit}}(k_{\text{Rec}}^*) = C'_{\text{Fit}}(k_{\text{Rec}}^*) * F_{\text{Bgd}}(k_{\text{Rec}}^*)$

447 3.7 Systematic uncertainties

448 In order to understand the systematic uncertainties of our data, the analysis code was run many times
 449 using slightly different values for a number of important cuts, and the results were compared. To quantify
 450 the systematic errors on the data, all correlation functions built using all varied cut values were bin-by-
 451 bin averaged, and the resulting variance of each bin was taken as the systematic error. The cuts included
 452 in the systematic study, as well as the values used in the variations, are shown in Tab. 4 (ΛK_S^0) and Tab.
 453 5 (ΛK^\pm). Note, the central value corresponds to that used in the analysis.

454 Similarly, the fit parameters extracted from all of these correlation functions were averaged, and the
 455 resulting variances were taken as the systematic errors for the fit parameters. As with the systematic
 456 errors on the data, this was performed for all varied cut values. Additionally, a systematic analysis
 457 was done on our fit method through varying our k^* fit range, as well as varying our modeling of the
 458 non-femtoscopic background. Our choice of k^* fit range was varied by $\pm 25\%$. As previously stated,
 459 the non-femtoscopic backgrounds are modeled using the THERMINATOR 2 simulation for the ΛK^\pm
 460 analyses, and with a linear form for the ΛK_S^0 system. To study the contribution of this choice to our
 461 systematic errors, we modeled the backgrounds of all of our systems by fitting to the data with a with a
 462 linear, quadratic, and Gaussian form. Additionally, we modeled the backgrounds of all systems with a
 463 polynomial fit to the THERMINATOR simulation, scaled to match the data. The resulting uncertainties
 464 in the extracted parameter sets were combined with our uncertainties arising from our particle and pair
 465 cuts.

ΛK_S^0 systematics

ΛK_S^0 systematics	
DCA $\Lambda(\bar{\Lambda})$	4, 5, 6 mm
DCA K_S^0	2, 3, 4 mm
DCA $\Lambda(\bar{\Lambda})$ Daughters	3, 4, 5 mm
DCA K_S^0 Daughters	2, 3, 4 mm
$\Lambda(\bar{\Lambda})$ Cosine of Pointing Angle	0.9992, 0.9993, 0.9994
K_S^0 Cosine of Pointing Angle	0.9992, 0.9993, 0.9994
DCA to Primary Vertex of $p(\bar{p})$ Daughter of $\Lambda(\bar{\Lambda})$	0.5, 1, 2 mm
DCA to Primary Vertex of $\pi^-(\pi^+)$ Daughter of $\Lambda(\bar{\Lambda})$	2, 3, 4 mm
DCA to Primary Vertex of π^+ Daughter of K_S^0	2, 3, 4 mm
DCA to Primary Vertex of π^- Daughter of K_S^0	2, 3, 4 mm
Average Separation of Like-Charge Daughters	5, 6, 7 cm

Table 4: ΛK_S^0 systematics ΛK^\pm systematics

ΛK^\pm systematics	
DCA $\Lambda(\bar{\Lambda})$	4, 5, 6 mm
DCA $\Lambda(\bar{\Lambda})$ Daughters	3, 4, 5 mm
$\Lambda(\bar{\Lambda})$ Cosine of Pointing Angle	0.9992, 0.9993, 0.9994
DCA to Primary Vertex of $p(\bar{p})$ Daughter of $\Lambda(\bar{\Lambda})$	0.5, 1, 2 mm
DCA to Primary Vertex of $\pi^-(\pi^+)$ Daughter of $\Lambda(\bar{\Lambda})$	2, 3, 4 mm
Average Separation of $\Lambda(\bar{\Lambda})$ Daughter with Same Charge as K^\pm	7, 8, 9 cm
Max. DCA to Primary Vertex in Transverse Plane of K^\pm	1.92, 2.4, 2.88
Max. DCA to Primary Vertex in Longitudinal Direction of K^\pm	2.4, 3.0, 3.6

Table 5: ΛK^\pm systematics

4 Results

Figure 5 shows our ΛK data with fits for all studied centrality bins (0-10%, 10-30%, and 30-50%). All analyses were fit simultaneously across all centralities, with a single radius and normalization λ parameter for each centrality bin. Scattering parameters ($\Re f_0$, $\Im f_0$, d_0) were shared between pair-conjugate systems, but assumed unique between the different ΛK charge combinations (i.e. a parameter set describing the ΛK^+ & $\bar{\Lambda}K^-$ system, a second set describing the ΛK^- & $\bar{\Lambda}K^+$ system, and a third for the ΛK_S^0 & $\bar{\Lambda}K_S^0$ system). Each correlation function received a unique normalization parameter. The fits were corrected for finite momentum resolution effects, non-femtoscopic backgrounds, and residual correlations resulting from the feed-down from resonances. In Fig. 5, lines represent statistical errors, while boxes represent systematic errors. The black solid curve shows the primary (ΛK) contribution to the fit, the green curve shows the fit to the non-femtoscopic background, and the purple curve shows the final fit after all corrections have been applied. The extracted fit values with uncertainties are printed as (fit value) \pm (statistical uncertainty) \pm (systematic uncertainty).

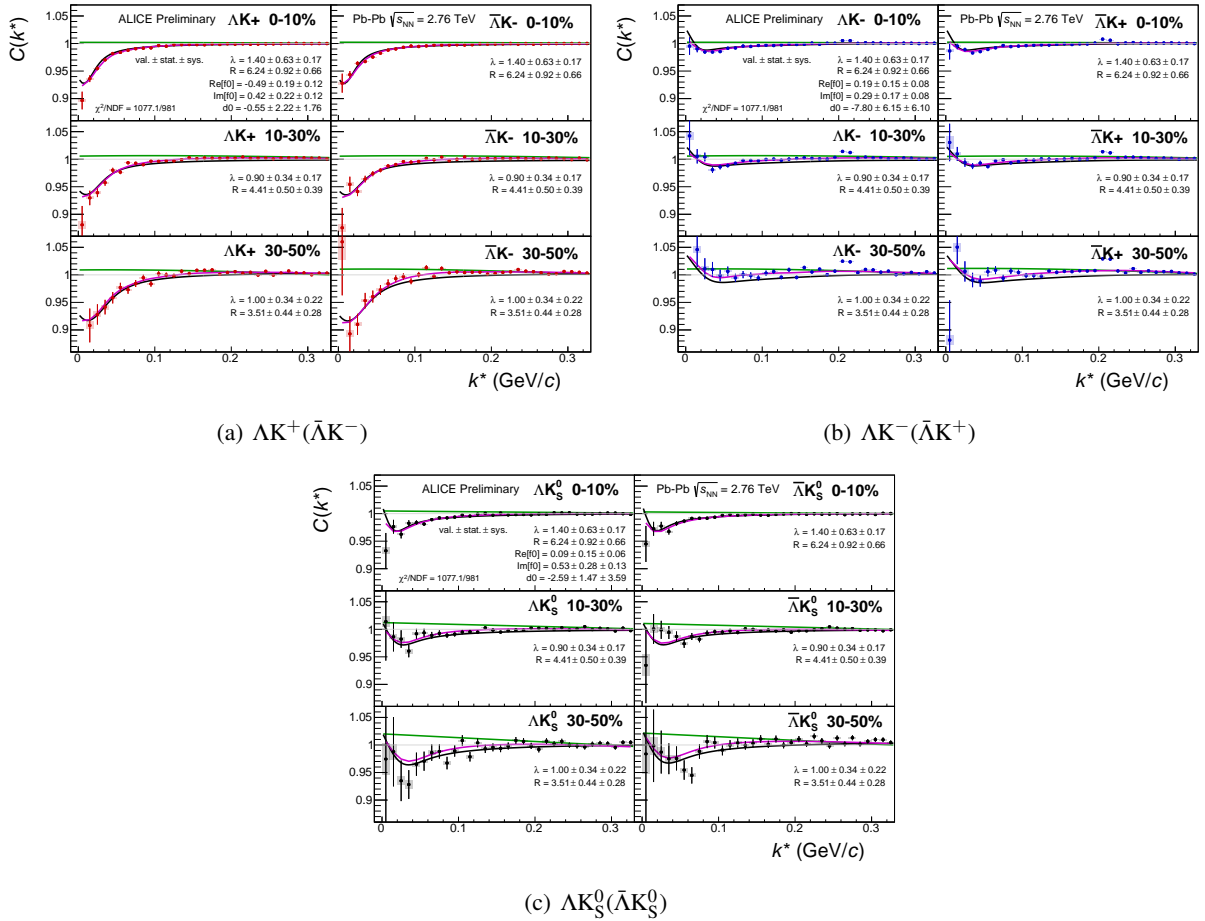


Fig. 5: Fits, with 3 residual correlations included, for all ΛK analyses across all studied centralities (0-10%, 10-30%, and 30-50%). The lines represent the statistical errors, while the boxes represent the systematic errors. The black solid line represents the primary (ΛK) correlation's contribution to the fit. The green line shows the fit to the non-flat background. The purple points show the fit after all residuals' contributions have been included, and momentum resolution and non-flat background corrections have been applied. The extracted fit values with uncertainties are printed.

Figure 6 summarizes well our results. In the summary plot, we show the extracted scattering parameters in the form of a $\Im f_0$ vs $\Re f_0$ plot, which includes the d_0 values to the right side. We also show the λ vs. radius parameters for all three of our studied centrality bins. In addition to our results, we show

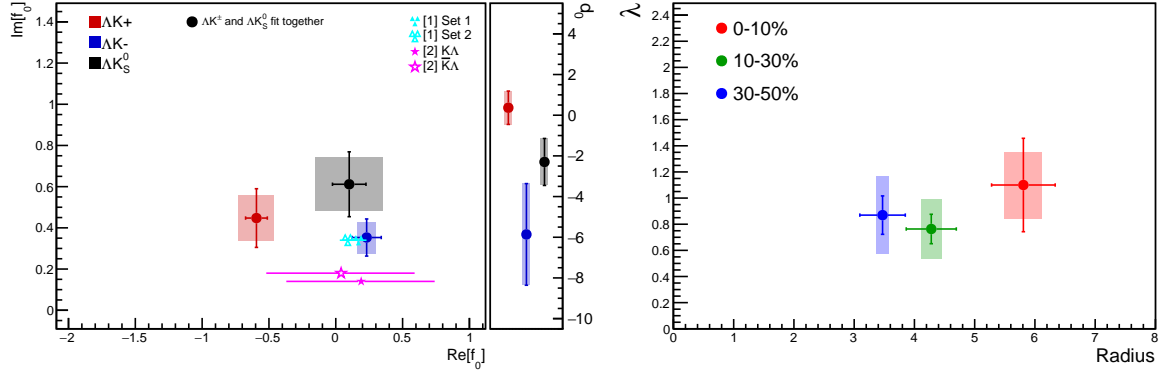


Fig. 6: Extracted scattering parameters for all of our AK systems. [Left]: $\Im(f_0)$ vs. $\Re(f_0)$, together with d_0 to the right. [Right]: λ vs. Radius for the studied centrality bins (0-10%, 10-30%, 30-50%). The green [19] and yellow [20] points show theoretical predictions made using chiral perturbation theory.

482 theoretical predictions made using chiral perturbation theory [19, 20].

483 We extract positive imaginary parts, $\Im(f_0)$, of the scattering lengths for all systems. We expect this,
484 as $\Im(f_0)$ describes the inelastic scattering channels. More interestingly, our results show that the ΛK^+
485 and ΛK^- systems differ in the sign of the real part, $\Re(f_0)$, of their scattering lengths (negative for
486 ΛK^+ , and positive for ΛK^-). Furthermore, each of the three systems has a $\Re(f_0)$ unique from the
487 others. The real part of the scattering length describes the effect of the strong interaction, making the
488 difference in these systems quite intriguing. A positive $\Re(f_0)$ signifies that the effect of the strong force
489 is attractive, which a negative $\Re(f_0)$ signifies a repulsion. We suggest that this difference could be due to
490 an effect arising from different quark-antiquark interactions between the pairs ($s\bar{s}$ in ΛK^+ , $u\bar{u}$ in ΛK^-).
491 An alternative explanation could be that the effect is due to the different net strangeness for each system.
492 More specifically, systems with less net strangeness have more channels into which they can decay,
493 causing a scarcity of pairs, i.e. a greater suppression of the correlation function, at low- k^* . However, an
494 effect such as this really should instead manifest itself in $\Im(f_0)$ not $\Re(f_0)$. In any case, this remains a
495 very interesting effect which needs an explanation.

496 A comparison of our extracted radii to those of other systems measure by ALICE [2] is shown in Figure
497 7. The figure shows extracted R_{inv} vs. m_T for several centralities and for several different systems. The
498 radii are observed to increase for more central events, as expected from a simple geometric picture of the
499 collisions. They also demonstrate a decreasing size with increasing m_T , as expected in the presence of
500 collective radial flow [3]. It was found that [4], even in the presence of good global m_T -scaling for the
501 three-dimensional radii in the LCMS frame, a particle species dependence will exist for the R_{inv} measured
502 in the PRF, due to trivial kinematic reasons. These kinematic effects, resulting from the transformation
503 from LCMS to PRF, causes smaller masses to exhibit larger R_{inv} [2] (explaining, for instance, how the
504 pion radii are systematically higher than kaon radii at the same approximate m_T).

505 It is clear from the results that the ΛK systems do not conform to the approximate m_T -scaling of the pair
506 source sizes.¹ At first thought, this may appear to be a troubling result; the approximate scaling is an

¹ For our non-identical particle pairs, to be more directly analogous to the single particle m_T , we define the pair transverse mass as

$$\begin{aligned} m_{T,\text{pair}}^2 &= \left(\frac{m_{\text{inv}}}{2}\right)^2 + \left(\frac{1}{2}|\mathbf{p}_{T,1} + \mathbf{p}_{T,2}|\right)^2 \\ &= (K^0)^2 - (K^3)^2 \\ \text{where } K^\mu &\equiv \frac{1}{2}(p_1^\mu + p_2^\mu) \end{aligned}$$

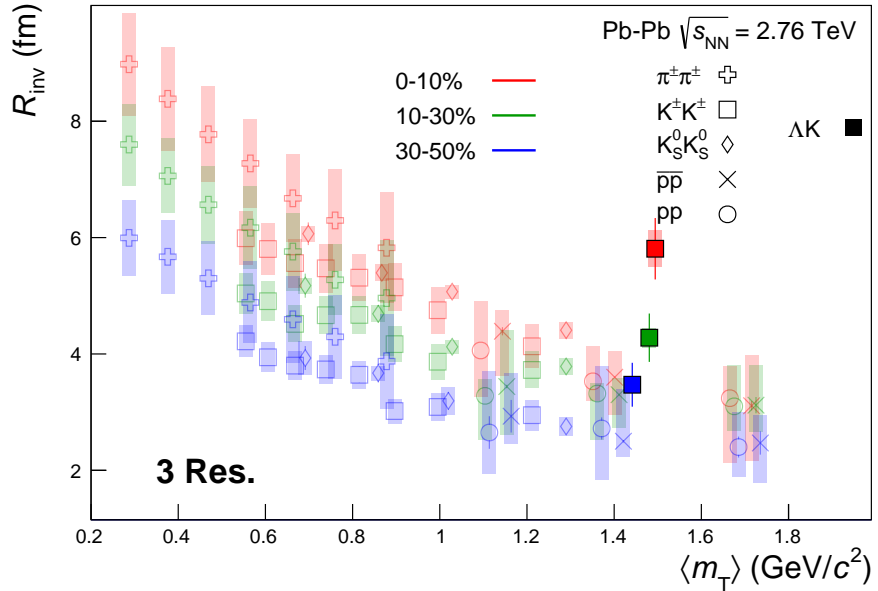


Fig. 7: 3 residual correlations in ΛK fits. Extracted fit R_{inv} parameters as a function of pair transverse mass (m_T) for various pair systems over several centralities. The ALICE published data [2] is shown with transparent, open symbols.

507 observed consequence of the collective behavior of the soft ($low-p_T$) sector of the produced system. The
 508 Λ and K particles certainly participate in the collective expansion of the QGP medium, but, importantly,
 509 they are non-identical particles. Taking a closer look at Fig. 7, one can see that the previously published
 510 data (transparent points), and the established (approximate) m_T -scaling trend, are for identical particle
 511 analyses only. When dealing with non-identical particles, the pair emission source, which is measured
 512 by femtoscopy, is the superposition of two single-particle sources. In general, each single-particle source
 513 will have its own size, shape, and space-time position within the produced medium, which is unique from
 514 its paired partner. The hydrodynamic nature of the medium produces the approximate m_T -scaling with
 515 respect to these single-particle sources, not the pair sources. The combination of two unique sources sep-
 516 arated in space-time, when probing correlations between non-identical particle pairs, leads to extracted
 517 radii falling outside of the (identical particle femtoscopy) m_T -scaling trend.

518 It is well established that non-identical particle femtoscopic studies are able to probe deeper than the
 519 second moments of the pair distribution functions accessed via identical particle studies. In addition to
 520 this, non-identical particle studies are able to measure the relative emission shifts, the first moments of the
 521 emission function. For the study of ΛK pairs at mid-rapidity in Pb-Pb collisions, we expect a separation
 522 of the single-particle sources in the out direction. One elegant method for extracting information about
 523 the emission asymmetries is via a spherical decomposition of the correlation function. With this method,
 524 one can draw a wealth of information from just a few components of the decomposition. Particularly, the
 525 C_{00} component is similar to the 1D correlation functions typically studied, and probes the overall size of
 526 the source. The $\Re C_{11}$ component probes the asymmetry of the system in the out direction; a non-zero
 527 value reveals the asymmetry. Figure D.1 in App. D shows the C_{00} and $\Re C_{11}$ components of the spherical
 528 decomposition of our ΛK^+ data in the 0-10% centrality bin. The $\Re C_{11}$ component shows a clear deviation
 529 from zero, and the negative value signifies that the Λ particles are, on average, emitted further out and/or
 530 earlier than the K mesons. This effect is supported by the results obtained from the THERMINATOR
 531 2 model, shown in Fig. E.1. The effect of a non-zero shift in the source will naturally lead to larger
 532 measured radii. This is intuitive, and also reaffirmed in our simulation with THERMINATOR 2 shown
 533 in App. E. We have also shown larger effective radii to result from inserting a Gaussian source with a
 534 non-zero shift into the Koonin-Pratt equation and numerically integrating.

535 **5 Summary**

536 Results from a femtoscopic analysis of ΛK correlations in Pb-Pb collisions at $\sqrt{s_{\text{NN}}} = 2.76$ TeV with
 537 ALICE at the LHC have been presented. The femtoscopic radii, λ parameters, and scattering param-
 538 eters were extracted from one-dimensional correlation functions in terms of the invariant momentum
 539 difference. The scattering parameters of ΛK pairs in all three charge combinations (ΛK^+ , ΛK^- , and
 540 ΛK_S^0) have been measured for the first time. We observe a striking difference in the ΛK^+ and ΛK^-
 541 correlation functions, which is reflected in the unique set of scattering parameters extracted for each.
 542 The ΛK^+ systems exhibits a negative $\Re(f_0)$, while that extracted from the ΛK^- system is positive. The
 543 physics underlying this phenomenon is currently not well understood, but we suggest this could be due
 544 to different quark-antiquark interactions between the pairs, or from different net strangeness for each
 545 system. Finally, we find that the ΛK systems exhibit source radii larger than expected from extrapolation
 546 from identical particle femtoscopic studies. We understand this effect to result from the separation in
 547 space-time of the single-particle Λ and K source distributions.

548 **Acknowledgements**

549 **References**

- 550 [1] M. A. Lisa, S. Pratt, R. Soltz, and U. Wiedemann, “Femtoscopy in relativistic heavy ion
 551 collisions,” *Ann. Rev. Nucl. Part. Sci.* **55** (2005) 357–402, [arXiv:nucl-ex/0505014](https://arxiv.org/abs/nucl-ex/0505014)
 552 [nucl-ex].
- 553 [2] **ALICE** Collaboration, J. Adam *et al.*, “One-dimensional pion, kaon, and proton femtoscopy in
 554 Pb-Pb collisions at $\sqrt{s_{\text{NN}}} = 2.76$ TeV,” *Phys. Rev.* **C92** no. 5, (2015) 054908, [arXiv:1506.07884](https://arxiv.org/abs/1506.07884)
 555 [nucl-ex].
- 556 [3] S. V. Akkelin and Yu. M. Sinyukov, “The HBT interferometry of expanding sources,” *Phys. Lett.*
 557 **B356** (1995) 525–530.
- 558 [4] A. Kisiel, M. Gaayn, and P. Boek, “Pion, kaon, and proton femtoscopy in Pb-Pb collisions at
 559 $\sqrt{s_{\text{NN}}}=2.76$ TeV modeled in (3+1)D hydrodynamics,” *Phys. Rev.* **C90** no. 6, (2014) 064914,
 560 [arXiv:1409.4571](https://arxiv.org/abs/1409.4571) [nucl-th].
- 561 [5] R. Lednický and V. L. Lyuboshits, “Final State Interaction Effect on Pairing Correlations Between
 562 Particles with Small Relative Momenta,” *Sov. J. Nucl. Phys.* **35** (1982) 770. [*Yad. Fiz.* **35**, 1316(1981)].
- 564 [6] **ALICE** Collaboration, K. Aamodt *et al.*, “The alice experiment at the cern lhc,” *JINST* **3** (2008)
 565 S08002. <http://stacks.iop.org/1748-0221/3/i=08/a=S08002>.
- 566 [7] **ALICE** Collaboration, B. Abelev *et al.*, “Centrality determination of Pb-Pb collisions at $\sqrt{s_{\text{NN}}} =$
 567 2.76 TeV with ALICE,” *Phys. Rev.* **C88** no. 4, (2013) 044909, [arXiv:1301.4361](https://arxiv.org/abs/1301.4361) [nucl-ex].
- 568 [8] J. Alme *et al.*, “The ALICE TPC, a large 3-dimensional tracking device with fast readout for
 569 ultra-high multiplicity events,” *Nucl. Instrum. Meth. A* **622** (2010) 316–367, [arXiv:1001.1950](https://arxiv.org/abs/1001.1950)
 570 [physics.ins-det].
- 571 [9] **ALICE** Collaboration, B. B. Abelev *et al.*, “Performance of the ALICE Experiment at the CERN
 572 LHC,” *Int. J. Mod. Phys.* **A29** (2014) 1430044, [arXiv:1402.4476](https://arxiv.org/abs/1402.4476) [nucl-ex].
- 573 [10] A. Akindinov *et al.*, “Performance of the ALICE Time-Of-Flight detector at the LHC,” *Eur. Phys.
 574 J. Plus* **128** (2013) 44.

- 575 [11] X.-N. Wang and M. Gyulassy, “HIJING: A Monte Carlo model for multiple jet production in pp,
576 pA, and AA collisions,” *Phys. Rev. D* **44** (Dec, 1991) 3501–3516.
577 <https://link.aps.org/doi/10.1103/PhysRevD.44.3501>.
- 578 [12] R. Brun, F. Bruyant, F. Carminati, S. Giani, M. Maire, A. McPherson, G. Patrick, and L. Urban,
579 “GEANT Detector Description and Simulation Tool,”
- 580 [13] **Particle Data Group** Collaboration, C. Patrignani *et al.*, “Review of Particle Physics,” *Chin.
581 Phys.* **C40** no. 10, (2016) 100001.
- 582 [14] S. E. Koonin, “Proton Pictures of High-Energy Nuclear Collisions,” *Phys. Lett.* **B70** (1977) 43–47.
- 583 [15] S. Pratt, T. Csorgo, and J. Zimanyi, “Detailed predictions for two pion correlations in
584 ultrarelativistic heavy ion collisions,” *Phys. Rev.* **C42** (1990) 2646–2652.
- 585 [16] A. Kisiel, H. Zbroszczyk, and M. Szymaski, “Extracting baryon-antibaryon strong interaction
586 potentials from p \bar{A} femtosscopic correlation functions,” *Phys. Rev.* **C89** no. 5, (2014) 054916,
587 [arXiv:1403.0433 \[nucl-th\]](https://arxiv.org/abs/1403.0433).
- 588 [17] M. Chojnacki, A. Kisiel, W. Florkowski, and W. Broniowski, “THERMINATOR 2: THERMal
589 heavy IoN generATOR 2,” *Comput. Phys. Commun.* **183** (2012) 746–773, [arXiv:1102.0273](https://arxiv.org/abs/1102.0273)
590 [nucl-th].
- 591 [18] A. Kisiel, “Non-identical particle correlation analysis in the presence of non-femtosopic
592 correlations,” *Acta Physica Polonica B* **48** (04, 2017) 717.
- 593 [19] Y.-R. Liu and S.-L. Zhu, “Meson-baryon scattering lengths in HB chi PT,” *Phys. Rev.* **D75** (2007)
594 034003, [arXiv:hep-ph/0607100 \[hep-ph\]](https://arxiv.org/abs/hep-ph/0607100).
- 595 [20] M. Mai, P. C. Bruns, B. Kubis, and U.-G. Meissner, “Aspects of meson-baryon scattering in three
596 and two-flavor chiral perturbation theory,” *Phys. Rev.* **D80** (2009) 094006, [arXiv:0905.2810](https://arxiv.org/abs/0905.2810)
597 [hep-ph].
- 598 [21] A. Stavinskiy *et al.*, “Some new aspects of femtoscopy at high energy,” *Nukleonika* **49**
599 (**Supplement 2**) (2004) S23.
- 600 [22] R. Lednický, “Finite-size effects on two-particle production in continuous and discrete spectrum,”
601 *Phys. Part. Nucl.* **40** (2009) 307–352, [arXiv:nucl-th/0501065 \[nucl-th\]](https://arxiv.org/abs/nucl-th/0501065).

602 A λ Parameters

AK ⁺ residuals		$\bar{\Lambda}K^-$ residuals		AK ⁻ residuals		$\bar{\Lambda}K^+$ residuals		AK _S ⁰ residuals		$\bar{\Lambda}K_S^0$ residuals	
Pair System	λ value	Pair System	λ value	Pair System	λ value	Pair System	λ value	Pair System	λ value	Pair System	λ value
3 Residuals (Max Parent $c\tau_{\text{decay}} = 10$ fm)											
AK ⁺	0.527	$\bar{\Lambda}K^-$	0.526	AK ⁻	0.526	$\bar{\Lambda}K^+$	0.527	AK _S ⁰	0.543	$\bar{\Lambda}K_S^0$	0.544
$\Sigma^0 K^+$	0.111	$\bar{\Sigma}^0 K^-$	0.110	$\Sigma^0 K^-$	0.110	$\bar{\Sigma}^0 K^+$	0.111	$\Sigma^0 K_S^0$	0.120	$\bar{\Sigma}^0 K_S^0$	0.120
$\Xi^0 K^+$	0.039	$\bar{\Xi}^0 K^-$	0.035	$\Xi^0 K^-$	0.038	$\bar{\Xi}^0 K^+$	0.036	$\Xi^0 K_S^0$	0.042	$\bar{\Xi}^0 K_S^0$	0.039
$\Xi^- K^+$	0.050	$\bar{\Xi}^+ K^-$	0.046	$\Xi^- K^-$	0.050	$\bar{\Xi}^+ K^+$	0.046	$\Xi^- K_S^0$	0.054	$\bar{\Xi}^+ K_S^0$	0.050
Other	0.226	Other	0.235	Other	0.228	Other	0.233	Other	0.194	Other	0.199
Fakes	0.048	Fakes	0.048	Fakes	0.048	Fakes	0.048	Fakes	0.048	Fakes	0.048
10 Residuals (Max Parent $c\tau_{\text{decay}} = 4$ fm)											
AK ⁺	0.180	$\bar{\Lambda}K^-$	0.180	AK ⁻	0.179	$\bar{\Lambda}K^+$	0.181	AK _S ⁰	0.192	$\bar{\Lambda}K_S^0$	0.193
$\Sigma^0 K^+$	0.116	$\bar{\Sigma}^0 K^-$	0.114	$\Sigma^0 K^-$	0.115	$\bar{\Sigma}^0 K^+$	0.116	$\Sigma^0 K_S^0$	0.125	$\bar{\Sigma}^0 K_S^0$	0.124
$\Xi^0 K^+$	0.040	$\bar{\Xi}^0 K^-$	0.037	$\Xi^0 K^-$	0.040	$\bar{\Xi}^0 K^+$	0.037	$\Xi^0 K_S^0$	0.043	$\bar{\Xi}^0 K_S^0$	0.040
$\Xi^- K^+$	0.052	$\bar{\Xi}^+ K^-$	0.047	$\Xi^- K^-$	0.052	$\bar{\Xi}^+ K^+$	0.048	$\Xi^- K_S^0$	0.056	$\bar{\Xi}^+ K_S^0$	0.052
$\Sigma^{*+} K^+$	0.054	$\bar{\Sigma}^{*-} K^-$	0.051	$\Sigma^{*+} K^-$	0.053	$\bar{\Sigma}^{*-} K^+$	0.051	$\Sigma^{*+} K_S^0$	0.058	$\bar{\Sigma}^{*-} K_S^0$	0.055
$\Sigma^{*-} K^+$	0.048	$\bar{\Sigma}^{*+} K^-$	0.050	$\Sigma^{*-} K^-$	0.048	$\bar{\Sigma}^{*+} K^+$	0.050	$\Sigma^{*-} K_S^0$	0.052	$\bar{\Sigma}^{*+} K_S^0$	0.054
$\Sigma^{*0} K^+$	0.048	$\bar{\Sigma}^{*0} K^-$	0.045	$\Sigma^{*0} K^-$	0.048	$\bar{\Sigma}^{*0} K^+$	0.045	$\Sigma^{*0} K_S^0$	0.052	$\bar{\Sigma}^{*0} K_S^0$	0.048
ΛK^{*0}	0.046	$\bar{\Lambda} \bar{K}^{*0}$	0.047	$\Lambda \bar{K}^{*0}$	0.046	$\bar{\Lambda} K^{*0}$	0.047	ΛK^{*0}	0.022	$\bar{\Lambda} K^{*0}$	0.022
$\Sigma^0 K^{*0}$	0.041	$\bar{\Sigma}^0 \bar{K}^{*0}$	0.041	$\Sigma^0 \bar{K}^{*0}$	0.041	$\bar{\Sigma}^0 K^{*0}$	0.041	$\Sigma^0 K^{*0}$	0.019	$\bar{\Sigma}^0 K^{*0}$	0.019
$\Xi^0 K^{*0}$	0.014	$\bar{\Xi}^0 \bar{K}^{*0}$	0.013	$\Xi^0 \bar{K}^{*0}$	0.014	$\bar{\Xi}^0 K^{*0}$	0.013	$\Xi^0 K^{*0}$	0.007	$\bar{\Xi}^0 K^{*0}$	0.006
$\Xi^- K^{*0}$	0.018	$\bar{\Xi}^+ \bar{K}^{*0}$	0.017	$\Xi^- \bar{K}^{*0}$	0.018	$\bar{\Xi}^+ K^{*0}$	0.017	$\Xi^- K^{*0}$	0.009	$\bar{\Xi}^+ K^{*0}$	0.008
Other	0.295	Other	0.310	Other	0.299	Other	0.307	Other	0.318	Other	0.330
Fakes	0.048	Fakes	0.048	Fakes	0.048	Fakes	0.048	Fakes	0.048	Fakes	0.048

Table A.1: λ values for the individual components of the AK correlation functions for the case of 3 and 10 residual contributions.

603 **B Stavinskiy Reference Method**

604 Another option for obtaining the reference distribution, $B(k^*)$, is to use, what we will refer to as, the
 605 “Stavinskiy method” [21]. The method was first proposed to handle the case of one event femtoscopy, and
 606 has been suggested for use in eliminating momentum conservation effects in the reference distribution
 607 [1]. The method is appropriate for collisions between symmetric projectiles, at sufficiently large energy,
 608 with a detector which is symmetrical with respect to the transition $\mathbf{r} \rightarrow -\mathbf{r}$. The purpose of our use
 609 of the Stavinskiy method is to rid the correlation functions of the non-femtoscopic background. More
 610 specifically, our intent is to handle background contributions from elliptic flow, and other sources having
 611 reflection symmetry in the transverse plane. With the Stavinskiy method, mixed-event pairs are not used
 612 for the reference distribution; instead, same-event pseudo-pairs, formed by rotating one particle in a real
 613 pair by 180° in the transverse plane, are used. This rotation rids the pairs of any femtoscopic correlation,
 614 while maintaining correlations due to elliptic flow (and other suitably symmetric contributors).

615 The results of correctly implementing such a procedure are shown in Figure B.1. The figure shows
 616 the Stavinskiy method does a very good job of ridding the ΛK^\pm correlations of their non-femtoscopic
 617 backgrounds. We also see the procedure does not work as well on the ΛK_S^0 system.

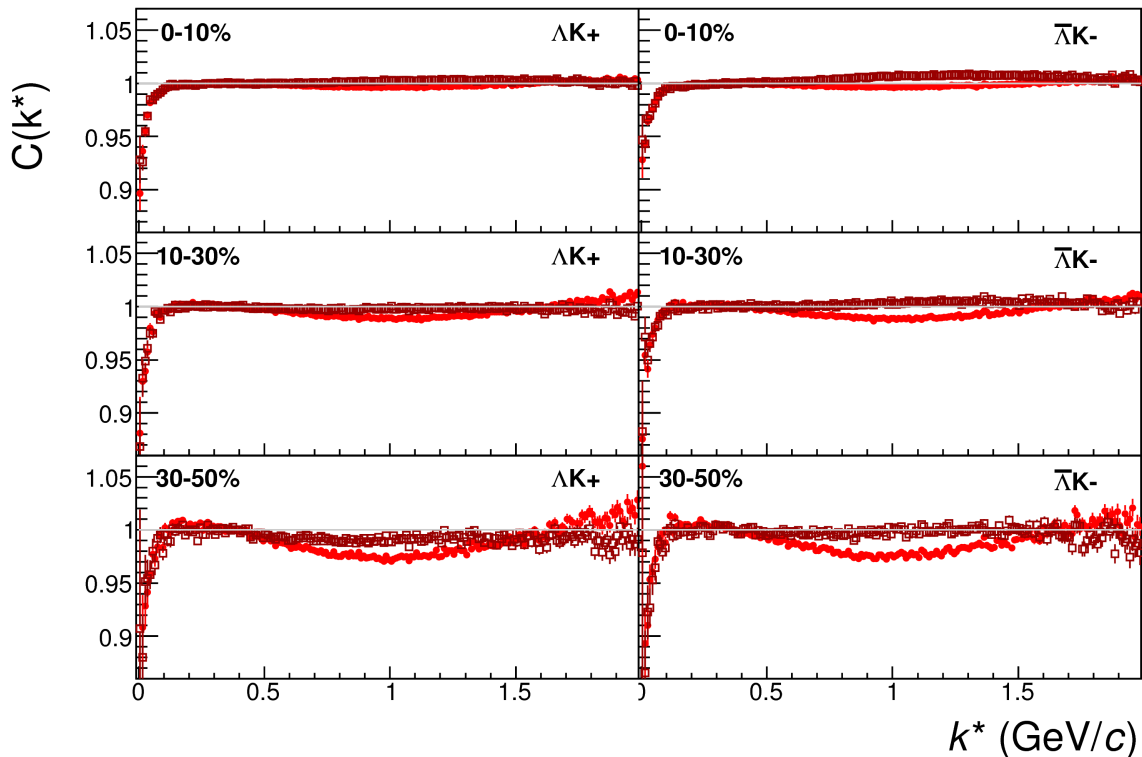


Fig. B.1: $\Lambda K^+(\bar{\Lambda} K^-)$ correlation functions built using the Stavinskiy method for 0-10%, 10-30%, and 30-50% centralities. Closed symbols represent correlations built using the normal mixed-event reference distribution, while open symbols represent correlations formed using the Stavinskiy same-event pseudo-pairs as a reference.

618 Now, one must be somewhat careful when applying this Stavinskiy method. We found that, in order to
 619 obtain correct results, we had to run our pseudo-pairs through the same pair cuts used in our analyses. In
 620 an ideal world, our pair cut would only remove truly bad pairs from splitting, merging, etc. In the
 621 real world, the pair cut always throws out some of the good with the bad. For the pseudo-pairs to form a
 622 reliable reference, they too must experience the pair cut, and the loss of “good” pseudo-pairs. We found
 623 this issue affected mainly our ΛK^+ & $\bar{\Lambda} K^-$ analysis.

624 **C Strong and Coulomb Fitter**

625 When modeling systems which include both strong and Coulomb effects, Eq. 7 is no longer valid, and, in
 626 fact, there is no analytical form with which to fit. To solve such a problem, and to fit such a system, one
 627 must develop a more fundamental model, beginning with Eq. 3 and using the two-particle wave-function
 628 including both strong and Coulomb interactions [22]:

$$\Psi_{\mathbf{k}^*}(\mathbf{r}^*) = e^{i\delta_c} \sqrt{A_c(\eta)} [e^{i\mathbf{k}^*\cdot\mathbf{r}^*} F(-i\eta, 1, i\xi) + f_c(k^*) \frac{\tilde{G}(\rho, \eta)}{r^*}] \quad (\text{C.1})$$

629 where $\rho = k^* r^*$, $\eta = (k^* a_c)^{-1}$, $\xi = \mathbf{k}^* \cdot \mathbf{r}^* + k^* r^* \equiv \rho(1 + \cos \theta^*)$, and $a_c = (\mu z_1 z_2 e^2)^{-1}$ is the two-
 630 particle Bohr radius (including the sign of the interaction). δ_c is the Coulomb s-wave phase shift, $A_c(\eta)$
 631 is the Coulomb penetration factor, $\tilde{G} = \sqrt{A_c}(G_0 + iF_0)$ is a combination of the regular (F_0) and singular
 632 (G_0) s-wave Coulomb functions. $f_c(k^*)$ is the s-wave scattering amplitude:

$$f_c(k^*) = [\frac{1}{f_0} + \frac{1}{2} d_0 k^{*2} - \frac{2}{a_c} h(\eta) - ik^* A_c(\eta)]^{-1} \quad (\text{C.2})$$

633 where, the “h-function”, $h(\eta)$, is expressed through the digamma function, $\psi(z) = \Gamma'(z)/\Gamma(z)$ as:

$$h(\eta) = 0.5[\psi(i\eta) + \psi(-i\eta) - \ln(\eta^2)] \quad (\text{C.3})$$

634 In this case, the λ parameter may be included as:

$$C(\mathbf{k}^*) = (1 - \lambda) + \lambda \int S(\mathbf{r}^*) |\Psi_{\mathbf{k}^*}^S(\mathbf{r}^*)|^2 d^3 \mathbf{r}^* \quad (\text{C.4})$$

635 To build a fit function for a system including both strong and Coulomb interactions we considered two
 636 related options. The first option was to numerically integrate Eq.3. The second option was to simulate
 637 a large sample of particle pairs, calculate the wave function describing the interaction, and average to
 638 obtain the integral in Eq.3. In either case, the solution would involve some very complicated mathemat-
 639 ical functions, as can be seen in Eqs. C.1 to C.3. Having no experience with either of these options, we
 640 elected the latter of simulating pairs.

641 **D Spherical Harmonic Decomposition**

642 In Fig. D.1 we show results for the C_{00} and $\Re C_{11}$ components from the spherical decomposition of our
 643 ΛK^+ system in the 0-10% centrality bin. As seen in the figure, the C_{00} signal is similar to that observed
 644 in our one-dimensional study. The $\Re C_{11}$ component shows a clear deviation from zero, and the negative
 645 value signifies that the Λ particles are, on average, emitted further out and/or earlier than the K mesons.

646 **E Relative Emission Shifts with THERMINATOR 2**

647 Fig. E.1 shows results from the THERMINATOR 2 event generator for an impact parameter of $b = 2$ fm.
 648 As THERMINATOR does not include any final state effects, the femtoscopic correlation was introduced
 649 by assuming a set of scattering parameters $(\Re f_0, \Im f_0, d_0) = (-1.16, 0.51, 1.08)$ and weighting the signal
 650 distribution (numerator pairs) with the modulus squared of the two-particle wave function, $|\Psi|^2$.

651 The top left of Fig. E.1(a) shows a fit to the one-dimensional correlation function from THERMINA-
 652 TOR 2. The scattering parameters are known precisely here, as they served as the weights used in the
 653 simulation, and are kept constant in the fit. We are interested in looking at the extracted one-dimensional

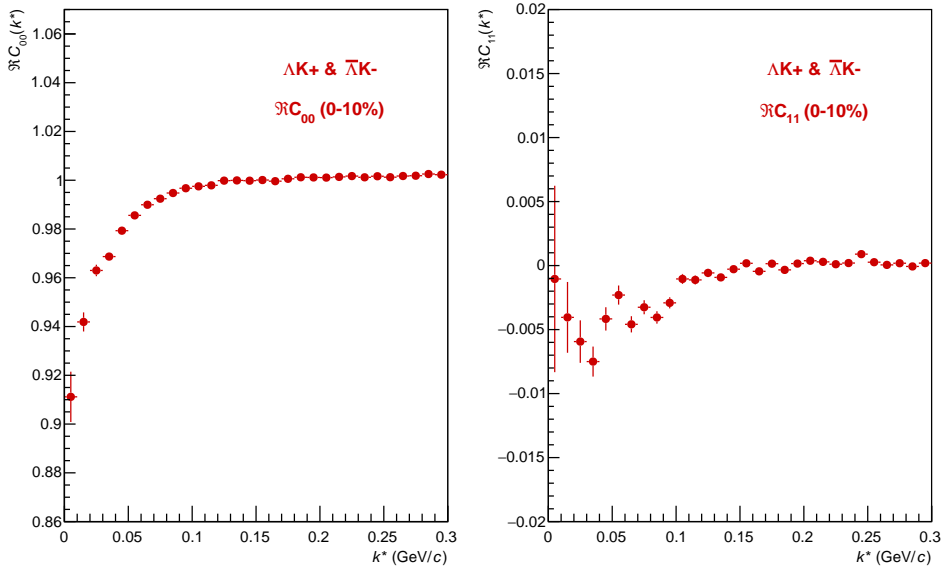
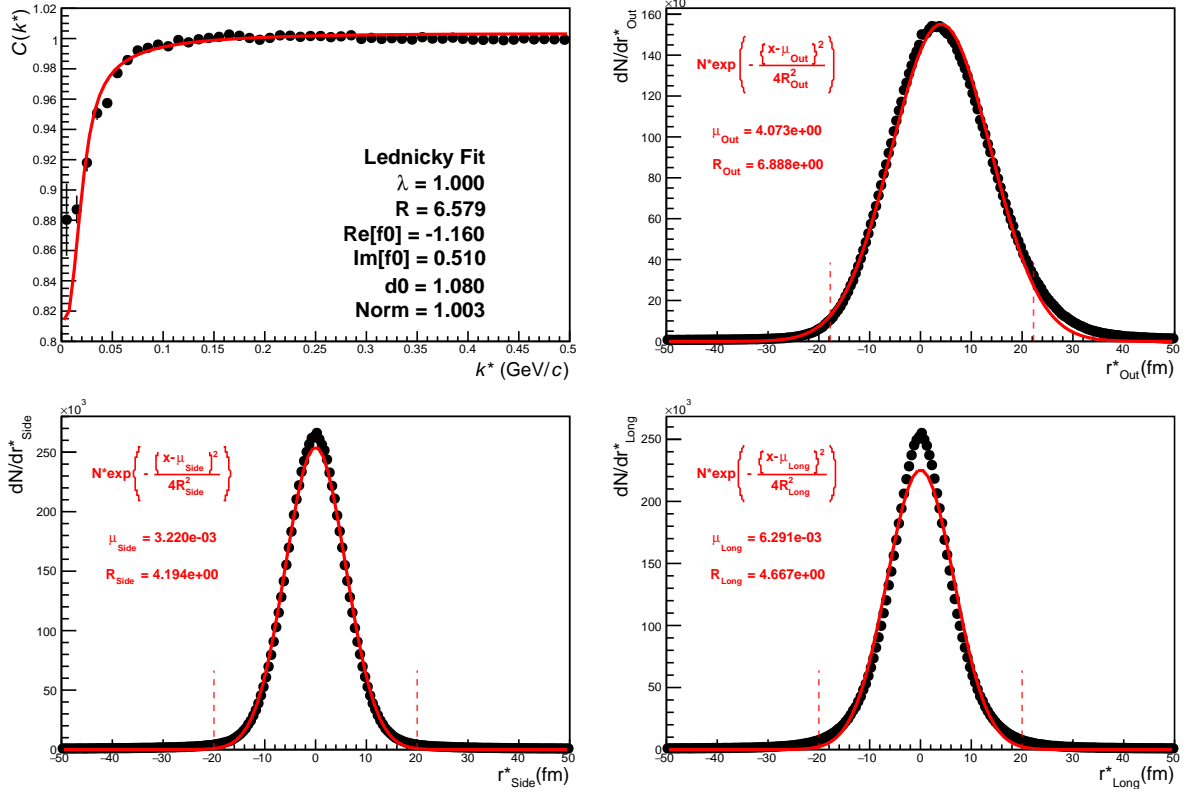


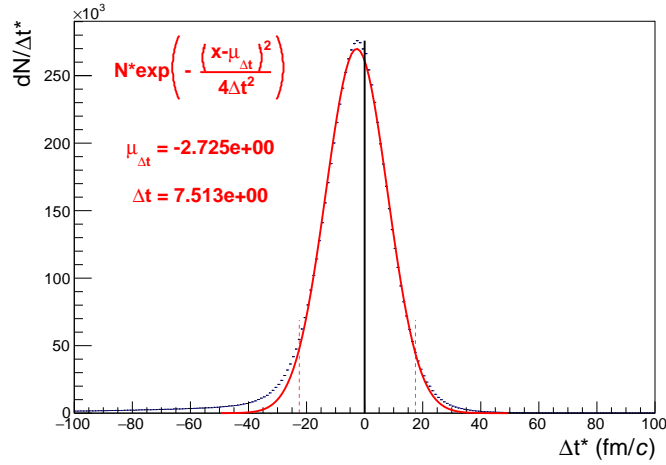
Fig. D.1: C_{00} (left) and $\Re C_{11}$ (right) components of a spherical harmonic decomposition of the ΛK^+ correlation function for the 0-10% centrality bin. The C_{00} component is similar to the 1D correlation functions typically studied, and probes the overall size of the source. The $\Re C_{11}$ component probes the asymmetry in the system; a non-zero value reveals the asymmetry

654 source size here, so the λ parameter is also fixed at unity. The other three plots in Fig. E.1(a) show the
 655 source distribution in the out (top right), side (bottom left), and long (bottom right) directions (all in the
 656 PRF). The source distributions have all been fitted with a Gaussian form, the result of which is printed
 657 within the respective plot. One immediately sees a significant shift in the out direction, $\mu_{\text{out}} \approx 4$ fm, and
 658 negligible shift in the other two directions, $\mu_{\text{side}} \approx \mu_{\text{long}} \approx 0$ fm. The figure demonstrates that, within
 659 the THERMINATOR 2 model, the Λ is, on average, emitted further out than its K partner. Finally, Fig.
 660 E.1(b) shows the distribution of the relative time of emittance, again in the PRF. The figure shows that
 661 the Λ is, on average, emitted earlier than its K partner.

662 We end this section with a brief look at how a spatial separation of the single particle sources affects
 663 the radii extracted from a femtoscopic analysis. To achieve this, we use THERMINATOR 2 in a similar
 664 fashion as described above, but with one important difference. Instead of taking the source information
 665 from THERMINATOR 2, we instead draw the source from a pre-determined Gaussian distribution. In
 666 all cases, we take $R_{\text{out}} = R_{\text{side}} = R_{\text{long}} = 5$ fm, and $\mu_{\text{side}} = \mu_{\text{long}} = 0$ fm. In Figure E.2, we show results
 667 for the case of $\mu_{\text{out}} = 1$ fm, $\mu_{\text{out}} = 3$ fm, and $\mu_{\text{out}} = 6$ fm. In this figure, we do not show the side and
 668 long distributions, as they are simple Gaussians of width 5 fm centered about the origin. The figure
 669 demonstrates that as the separation μ_{out} increases, so do the extracted femtoscopic radii.



(a) (Top Left) Simple fit on simulation from THERMINATOR 2. Generated source in the (Top Right) out, (Bottom Left) side, and (Bottom Right) long directions.



(b) Temporal characteristics of the source.

Fig. E.1: Extracted radius when performing a simple fit on simulation from THERMINATOR 2, along with the spatio-temporal characteristics generated by the simulation.

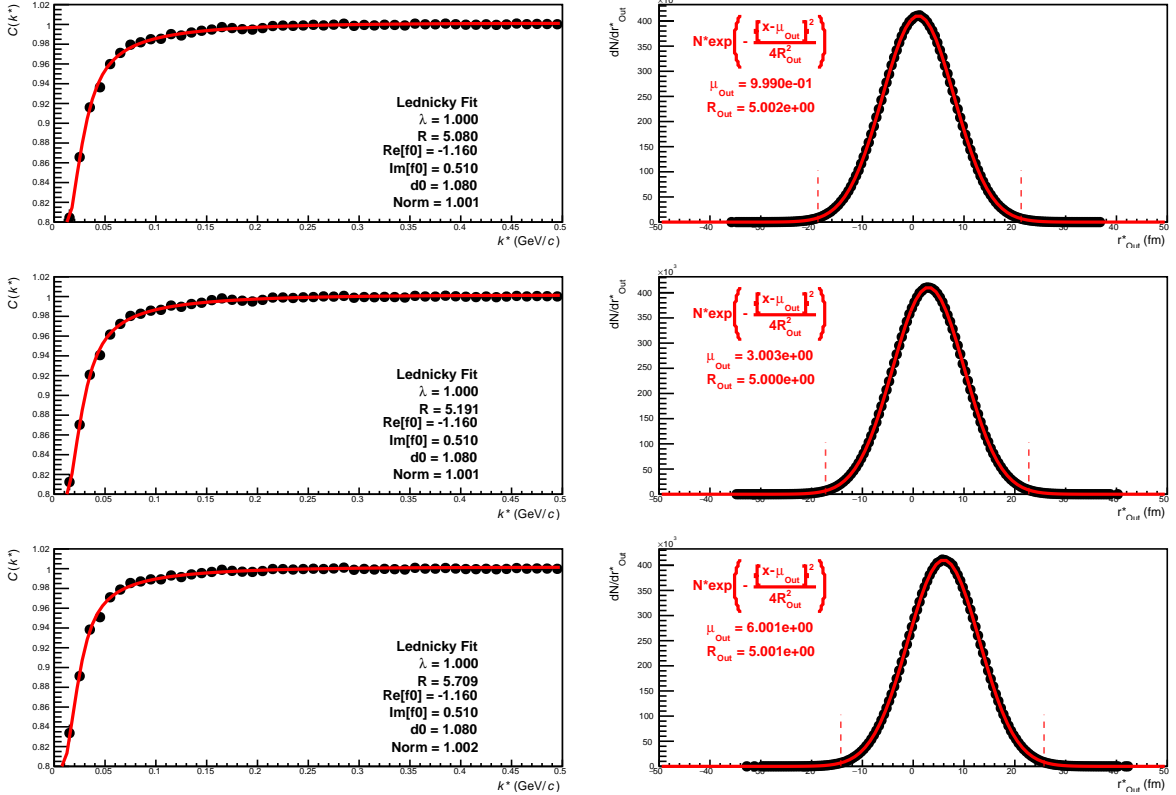


Fig. E.2: Probing the effect of varying the source shift in the outward direction, μ_{Out} , within the THERMINATOR 2 framework. To achieve this, we formed particle pairs from the simulation, but altered their spatial characteristics by drawing the out, side, and long components from pre-determined Gaussian distributions. The plots on the left show fits resulting from the sources (in the out direction) shown on the right. The sources in the side and long directions are not shown, and are both Gaussians of width 5 fm centered at the origin for all cases. Moving from top to bottom, μ_{Out} increase from 0 to 6 fm, the effect of which clearly increases the effective radius extracted in the fit.

670 **F The ALICE Collaboration**